Solar Physics
DOI: 10.1007/•••••-•••-•••-••••-•

Comparative Study of the Three-dimensional Thermodynamical Structure of the Inner Corona of Solar Minimum Carrington Rotations 1915 and 2081

Diego G. Lloveras[1,2] · Alberto M. Vásquez[1,3,2] · Federico A. Nuevo[1,2] · Richard A. Frazin[4]

Abstract Using differential emission measure tomography (DEMT) based on time series of EUV images, we carry out a quantitative comparative analysis of the the three-dimensional (3D) structure of the electron density and temperature of the inner corona ($r < 1.25\,\mathrm{R}_\odot$) between two specific rotations selected from the last two solar minima, namely Carrington rotations (CR-)1915 and CR-2081. The analysis places error bars in the results due to systematic uncertainty sources. While the results for CR-2081 are characterized by a remarkable northern/southern symmetry, for CR-1915 the southern hemisphere exhibits larger densities and temperatures than its northern one. For both rotations the core region of the streamer belt is found to be populated by structures with temper-

✉ D.G. Lloveras
dlloveras@iafe.uba.ar

✉ A.M. Vásquez
albert@iafe.uba.ar

✉ F.A. Nuevo
federico@iafe.uba.ar

✉ R.A. Frazin
rfrazin@umich.edu

[1] Instituto de Astronomía y Física del Espacio (IAFE), CONICET-UBA, CC 67 - Suc 28, (C1428ZAA) Ciudad Autónoma de Buenos Aires, Argentina.

[2] Departamento de Física, Facultad de Ciencias Exactas y Naturales (FCEN), Universidad de Buenos Aires (UBA), Pabellón I, Ciudad Universitaria, (C1428ZAA) Ciudad Autónoma de Buenos Aires, Argentina.

[3] Departamento de Ciencia y Tecnología, Universidad Nacional de Tres de Febrero (UNTREF), Valentín Gómez 4752, (B1678ABH) Caseros, Provincia de Buenos Aires, Argentina.

[4] Department of Climate and Space Sciences and Engineering (CLaSP), University of Michigan, 2455 Hayward Street, Ann Arbor, MI 48109-2143, USA.

ature decreasing with height (so-called "down loops" in our previous articles), characterized by plasma $\beta \gtrsim 1$, which may be the result of efficient dissipation of Alfvén waves at low coronal heights. The comparative analysis reveals that the low latitudes of the equatorial streamer belt of CR-1915 exhibit larger densities than for CR-2081 that cannot be explained by the systematic uncertainties. Also, the southern hemisphere of the streamer belt of CR-1915 is characterized by larger temperatures and density scale heights than for CR-2081. On the other hand, the coronal hole region of CR-1915 shows lower temperatures than for CR-2081. The reported differences are in the range $\approx 10 - 25\%$, depending on the specific physical quantity and region being compared, as fully detailed in the analysis. For other regions and/or physical quantities the uncertainties do not allow assessment of thermodynamical differences between the two rotations. Future investigation will involve DEMT analysis of other Carrington rotations selected from both epochs, and comparison of their tomographic reconstructions with magnetohydrodynamical simulations of the inner corona.

Keywords: Solar Cycle, Observations; Corona, E; Corona, Structures

1. Introduction

Advancement of the empirical knowledge of the three-dimensional (3D) structure of the large scale global corona is needed to validate 3D magnetohydrodynamic (MHD) models, and increase their capacity of predicting its large-scale behavior. In this regard, current important open areas of active research include the investigation of the origin of the solar wind, and the improvement of the ability of Sun-Earth models to predict space weather conditions. Towards these general goals, study of solar minima is particularly important, as they are the periods when the corona exhibits its simpler global configuration, thus providing to investigators the best opportunities to focus on large-scale features.

The sunspot number (SSN), a standard indicator of the activity level of the solar corona, has shown a systematic decline over the last three solar cycles (SC) 22, 23, and 24 (the current one)[1], along with others indicators such as the solar radio flux at 10.7 cm. The SC 23/24 minimum was particularly extended, exhibiting a very low level of activity for almost one full year, between the years 2008 and 2009. During that period, several rotations actually showed virtually no sunspots at all. In contrast, the previous SC 22/23 minimum was much shorter, more active, and during that epoch the time series of the SSN exhibited a stronger variability between consecutive rotations than during the SC 23/24 minimum. The SC 23/24 minimum exhibited also an overall weaker magnetic field than the previous minimum. As detailed at the beginning of Section 2, in this work we specifically analyze Carrington rotation (CR-)1915 from the SC 22/23 minimum, and CR-2081 from the SC 23/24 minimum.

Differences of the large scale structure of the solar corona during the last two activity minima have also been observed. Based on total and polarized white

[1] http://solarscience.msfc.nasa.gov/images/Cycle22Cycle23Cycle24big.gif

light (WL) images of the K corona taken by the Large Angle and Spectrometric Coronagraph (LASCO-C2) on board the SOlar and Heliospheric Observatory (SOHO) mission, Lamy *et al.* (2014) have reported systematic differences in the coronal WL radiance during the last two minima. They found the WL radiance of the SC 23/24 minimum to have been significantly lower than during the SC 22/23 minimum, with observed differences depending on the polar angle.

To study the global corona 3D structure, solar rotational tomography (SRT) constitutes a powerful tool. Originally developed by Altschuler and Perry (1972) to reconstruct the 3D distribution of the coronal electron density from WL coronagraph images, SRT relies on the solar rotation to allow instruments to collect a time-series of images that cover the full corona. Originally, SRT assumes a static corona (Frazin, 2000; Frazin and Janzen, 2002), although there are more recent time-dependent implementations (Butala *et al.*, 2010; Vibert *et al.*, 2016).

More recently, Frazin, Vásquez, and Kamalabadi (2009) developed differential emission measure tomography (DEMT), a SRT technique based on EUV images, that allows the study of the 3D thermodynamical structure of the quiet-Sun low corona at a global scale. As summarized in Section 2, using full solar rotation time series of EUV images taken in channels sensitive to different temperatures, DEMT allows calculation of 3D maps of both the electron density and temperature in the heliocentric height range 1.02 to 1.23 $\mathrm{R}_{\odot}$.

Complementary, the coronal magnetic field of the global corona can be modeled by means of potential field source surface (PFSS), or even MHD models. Combination of the DEMT and global magnetic models has provided useful insight in the 3D thermodynamical structure of the global quiet-Sun corona (Huang *et al.*, 2012; Nuevo *et al.*, 2013, 2015). A recent review of DEMT by Vásquez (2016) describes the technique and summarizes all published literature based on it.

Motivated by the differing characteristics of the last two solar minima, in this work we carry out a quantitatively detailed comparative DEMT and PFSS analysis of the selected rotations. To study CR-1915 data taken by the Extreme ultraviolet Imaging Telescope (EIT) on board SOHO was used. To study CR-2081 data taken by the Extreme UltraViolet Imager (EUVI) on board the Solar TErrestrial RElations Observatory (STEREO) mission was used. For both rotations, the PFSS models were computed based on synoptic magnetograms from data taken by the Michelson Doppler Imager (MDI) on board SOHO, using the Level 1.8 definitive calibration files provided by the data archive of the instrument.

Section 2 summarizes the techniques, instruments and data sets used. Section 3 details the results of both reconstructions separately, both in terms of the EUV emissivity (Section 3.1) and the thermodynamical state of the corona (Section 3.2). Section 3.3 explains in detail the technique that is used to trace the DEMT results along the field lines of the PFSS models. In Section 3.4 the solar corona is dissected in regions for analysis in both rotations, and in Section 3.5 the quantitative comparative analysis of both rotations is shown. In Section 4 different types of temperature structures are classified and analyzed in both rotations. Section 5 summarizes and discusses the main conclusions of this analysis, and anticipates further planned work. Finally, Appendix A details a study of the main systematic uncertainties that affect the DEMT results.

2. Data and Methodology

To perform the comparison two specific rotations were selected from each minimum, namely CR-1915 (1996, 15 October through 11 November) and CR-2081 (2009, 09 March through 05 April). As DEMT aims at studying the quiet-Sun corona, solar rotations showing the lowest possible number of SSNs were selected from each minimum. CR-1915 was chosen for analysis as, belonging to the deep minimum period of the smoothed monthly averaged Brussels International SSN (1996, March through November), it marked the absolute minimum (a value of 0.9) of the monthly averaged time series.[2] This selected rotation was also very close to the first Whole Sun Month (WSM) campaign period (CRs 1912-1913, Biesecker *et al.* 1999). It was also one of the ones of that period for which the EIT database had best full-rotation coverage which, being an important requirement for DEMT analysis, was not nearly as uniform during SC 22/23 as the EUVI database was during SC 23/24. CR-2081 was chosen as, also belonging to the respective deep minimum period of the smoothed monthly averaged SSN (July 2008 through June 2009), it marked the absolute minimum (a value of 0.7) of the monthly averaged SSN.

To determine the thermodynamical structure of both rotations, the DEMT technique was applied to respective time series of EUV images covering each rotation in full. To study CR-1915 and CR-2081 data taken by the EIT/SOHO and EUVI/STEREO instruments was used, respectively.

In DEMT, the low corona in the height range 1.0 to 1.25 $R_\odot$ is discretized in a spherical computational grid. The size of the tomographic cell (or voxel) is set to 0.01 $R_\odot$ in the radial direction, while is set 2° in both the latitudinal and longitudinal directions. With this angular resolution one image every 6 hours is the cadence needed to fully constrain the inversion problem, for a total of about 110 images to cover a full solar rotation. We refer the reader to Frazin, Vásquez, and Kamalabadi (2009) for a detailed description of the technique, and to Vásquez (2016) for a recent review on all published work based on it. Here we summarize the key points. The technique involves two consecutive procedures.

In a first step, the time series of EUV images is used to solve a SRT problem, for each EUV band independently. As a result, the 3D distribution of the so called filter band emissivity (FBE) is determined for each band separately. The FBE, an emissivity-type quantity, is defined as the wavelength integral of the coronal EUV spectral emissivity and the telescope's passband function of each EUV channel. Line-of-sight (LOS) integration of the FBE provides synthetic images that can be quantitatively compared to the real data in the time series. To find the FBE, the tomographic problem is posed a global optimization problem in which the quadratic norm of the difference between all pairs of synthetic and real images is minimized. Spatial regularization terms are also included in the objective function as to minimize high frequency spurious artifacts that are due to the specific characteristics of the SRT sparse projection matrix (Frazin, Vásquez, and Kamalabadi, 2009; Frazin, 2000). Due to optical depth issues that

[2]ftp://ftp.swpc.noaa.gov/pub/weekly/RecentIndices.txt

may affect LOSs passing very close to the limb, and to the decay of intensity with radii, the 3D maps produced by DEMT analysis typically cover the height range 1.02 to 1.23 $R_\odot$ (Frazin, Vásquez, and Kamalabadi, 2009).

In a second step, the FBE values obtained for all bands in each voxel are used to constrain the determination of a local differential emission measure (LDEM) distribution, which describes the temperature distribution of the electron plasma contained in each individual tomographic grid voxel. Specifically, at each tomographic voxel i, the FBE of the band k is related to the LDEM of the voxel according to

$$\mathrm{FBE}_i^{(k)} = \int dT\, \mathrm{LDEM}_i(T)\, \mathrm{TRF}^{(k)}(T), \quad k = 1, ..., K \tag{1}$$

where $\mathrm{TRF}^{(k)}(T)$ is the temperature response function (TRF) of the k-th detector, and $K = 3$ in the case of the instruments used in this work (EIT and EUVI). This relationship is equivalent to the one in standard DEM analysis relating the intensity of a specific spectral line with the contribution function of the line $G(T)$ and the DEM(T). The difference is that while the DEM(T) represents the temperature distribution of the plasma along the line-of-sight associated to a pixel, the LDEM(T) represents the distribution within the volume of a tomographic voxel.

The TRF at temperature T is calculated as the wavelength integral the known channel's passband times the coronal emissivity at that temperature (normalized by the squared electron density), which is computed by means of a coronal emission model. In this work the TRF of each EUV channel, of both EIT and EUVI, was computed for constant density (as in Frazin, Vásquez, and Kamalabadi 2009) with version 7.1 of the CHIANTI atomic data base (Landi *et al.*, 2013), using the abundance set `sun_coronal_feldman_1992_ext.abund` (Landi, Feldman, and Dere, 2002; Feldman *et al.*, 1992). The TRFs are similar to those shown in Figure 2 of Frazin, Vásquez, and Kamalabadi (2009), and their characteristic temperatures are those tabulated in Table 1 of Nuevo *et al.* (2015). Note that upper transition region Si VII emission at $T < 10^6$ MK, known to affect on-disk pixel intensities in the 284 band images of both the EIT and EUVI instruments, may be significant only in the voxels of the lowest height range $1.0 - 1.02\,R_\odot$, which are left out of the DEMT analysis. Si VII may provide emission in voxels at larger heights along large, cold loops of ARs, but those regions are also left out of the analysis.

DEM inversion problems are difficult to treat due to their ill-posed nature. When based on high-resolution spectral data, DEM analysis can be performed through the Monte Carlo Markov Chain (MCMC) approach (Kashyap and Drake, 1998), regularized inversion techniques (Hannah and Kontar, 2012). More recently, a sparse Bayesian inference method to study the coronal temperature structure was introduced by Warren, Byers, and Crump (2017). In the case of narrow band images, parametrization of the DEM is a suitable approach. For example, parametric DEM studies related to active regions have been carried out by Aschwanden and Boerner (2011), Plowman, Kankelborg, and Martens (2013), and Del Zanna (2013). Also, a new fast DEM inversion method for AIA

images based on the concept of sparsity was recently proposed by Cheung *et al.* (2015).

DEMT makes use of parametric models for determination of the LDEM. Nuevo *et al.* (2015) have validated the parametric technique used in DEMT by comparing its results when applied to standard DEM analysis of EUV images against those obtained by studies using MCMC techniques. Future new developments in DEMT may explore the implementation of regularized inversion techniques for the determination of the LDEM at each voxel, or even MCMC methods as applied to AIA images by Schmelz, Christian, and Chastain (2016).

When using data from 3 EUV bands, as in the case of EIT and EUVI, a Gaussian model for the LDEM is able to accurately predict the tomographic emissivities (Frazin, Vásquez, and Kamalabadi, 2009; Nuevo *et al.*, 2015). In each tomographic voxel the problem is then reduced to finding the values of the three free parameters of the Gaussian (centroid, standard deviation, and area) that allow to best reproduce the three tomographically reconstructed values of FBE in that voxel. To do so, an objective function is defined that measures the quadratic differences between tomographically determined FBE values and those synthesized from the modeled LDEM.

Once the LDEM is determined at each voxel, the average squared electron density N_e^2 and the electron mean temperature T_m in the voxel can be computed by taking its zeroth and first moments over temperature. More specifically, at the i-th voxel,

$$N_{e,i}^2 = \int dT\, \mathrm{LDEM}_i(T), \tag{2}$$

$$T_{m,i} = \frac{1}{N_{e,i}^2} \int dT\, T\, \mathrm{LDEM}_i(T), \tag{3}$$

so that the final product of DEMT is in the form of 3D maps of the electron density and mean temperature. Once again, these relationships (derived in detail in Frazin, Vásquez, and Kamalabadi 2009, see Appendix C) are similar to those in standard DEM analysis, in which the line-of-sight DEM appears instead of the voxel's LDEM, and the EM appears instead of the squared electron density.

For the derivation of Equations (1)-(3) (or their equivalents in standard DEM analysis), the so called coronal approximation is assumed, according to which the coronal EUV emissivity is essentially due to ions being excited from ground level by collisions with free electrons. The emissivity can then be factorized as the local squared electron density times a sum of contribution functions that depend on the local electron temperature. As the EUV emission detected by the channels of both instruments is dominated by iron lines, the computed TRF is proportional to the assumed iron abundance [Fe]. The LDEM in each voxel scales then as $1/[\mathrm{Fe}]$, and hence the electron density calculated with Equation (2) scales as $N_{e,i} \propto 1/\sqrt{[\mathrm{Fe}]}$, while the electron mean temperature $T_{m,i}$ calculated with Equation (3) is not affected by [Fe].

Finally, a measure of the degree of success of the LDEM in reproducing the tomographically reconstructed FBEs is computed at each voxel,

$$R_i \equiv (1/K) \sum_{k=1}^{K} \left| 1 - \mathrm{FBE}_{i,\mathrm{syn}}^{(k)} / \mathrm{FBE}_{i,\mathrm{tom}}^{(k)} \right| , \tag{4}$$

where $\mathrm{FBE}_{i,\mathrm{tom}}^{(k)}$ is the tomographic FBE value for the band k, and $\mathrm{FBE}_{i,\mathrm{syn}}^{(k)}$ is the emissivity synthesized from LDEM_i by means of Equation (1). A perfect match of the tomographic and synthetic FBEs for all three EUV bands implies $R = 0$. Increasingly larger values of the score R measure a progressively larger disagreement between the tomographic and synthetic FBEs.

Independently of the DEMT analysis, an extrapolation of the photospheric magnetic field is carried out to model the global coronal magnetic field. For both selected rotations, the magnetic field was modeled by means of a potential field source surface (PFSS) model developed by Tóth, van der Holst, and Huang (2011), based on a finite differences numerical approach. In both cases the PFSS model was constrained by synoptic magnetograms built from data taken by the MDI/SOHO instrument.

Combination of the DEMT results with the PFSS models allows determination of the electron density and temperature along individual magnetic field lines. To that end, the geometry of the field lines is determined by numerical integration of the first order differential equations $\mathrm{d}r/B_r = r\mathrm{d}\theta/B_\theta = r\,\sin(\theta)\,\mathrm{d}\phi/B_\phi$, both inwards and outwards, from the specified 3D coordinates of a starting point. In order to evenly sample the whole volume spanned by the DEMT reconstructions, one starting point is selected at the center of each tomographic cell at 10 uniformly spaced heights, ranging from 1.03 to $1.21\,\mathrm{R}_\odot$, and every 2° in both latitude and longitude, for a total of 162,000 starting points. Each traced field line is classified as "open" if it intersects the source surface, set in this work at $r = 2.5\,\mathrm{R}_\odot$ (where lines become radial), or as "closed" otherwise. In the case of closed magnetic field lines, loops are further classified as "small" and "large" upon their apex height being within or beyond the range of heights studied by DEMT, respectively.

At this stage, all DEMT products, electron density and mean temperature in particular, can be traced along open and closed magnetic field lines. Once the field line geometry is computed in high spatial resolution, only one sample point per tomographic cell is kept (the median one). To each sample point, the DEMT results corresponding to the tomographic voxel where it is located are assigned to it. As a result, for each field line one data point per tomographic cell is obtained. This allows to analyze how the DEMT density and temperature vary with height along each individual field line. This approach was firstly used by Huang *et al.* (2012, hereafter Paper I) to study inverted temperature structures in the solar minimum corona, and later on applied by Nuevo *et al.* (2013, hereafter Paper II) to expand that analysis to rotations with different level of activity.

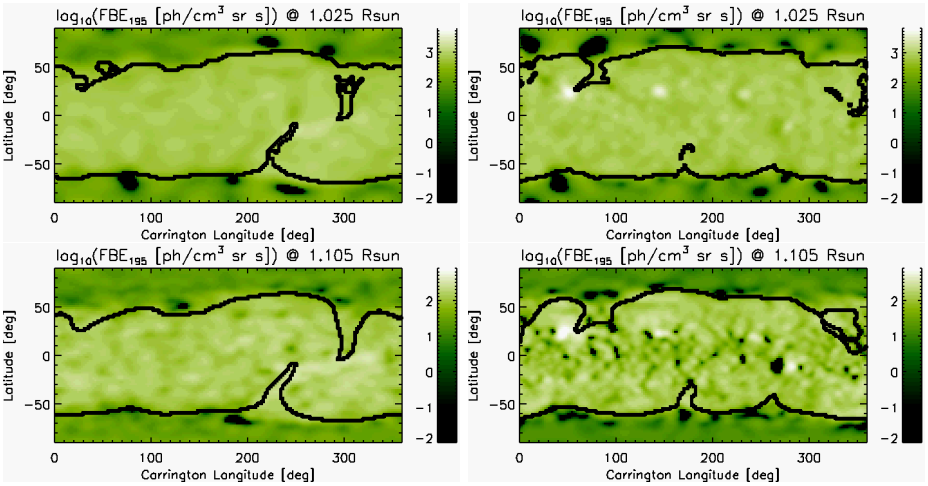

Figure 1. Carrington maps of the reconstructed FBE [ph cm^{-3} sr^{-1} s^{-1}] of the 195 Å band, for CR-1915 based on EIT data (left panels) and for CR-2081 based on EUVI data (right panels). Top and bottom panels show the results at two sample heliocentric heights, 1.025 and 1.105 R$_\odot$, respectively. Black voxels correspond to non-reconstructed regions (see text). In each panel the thick black curves indicate to the boundary between magnetically open and closed regions, as derived from the PFSS model.

3. Results: The Global Corona

3.1. 3D EUV Emissivity

The tomographic reconstruction of all EUV bands was performed for the two selected rotations. As a result the 3D distribution of the FBE of each band was determined. As an example, Figure 1 shows for both rotations the 195 Å FBE at two sample heights of the tomographic computational grid. The results are shown as Carrington maps, which display the distribution of the reconstructed quantity in latitude and longitude for the selected height. Similar maps were obtained at all heights of the tomographic grid, for all three EUV bands. In these maps, the thick-black curves indicate the open/closed boundaries of the corresponding PFSS model. Note how the magnetically closed region, that corresponds to the equatorial streamer belt, is characterized by larger values of FBE compared to the open regions, which hereafter define the coronal hole (CH) regions in the context of this study.

Due to unresolved coronal dynamics, tomographic reconstructions exhibit negative values of the reconstructed FBE, or zero when the solution is constrained to positive values (Frazin, 2000; Frazin, Vásquez, and Kamalabadi, 2009). These non-reconstructed voxels are indicated in black in the Carrington maps of reconstructed FBE.

Based on the 3D FBE maps for all three bands, the LDEM was determined in each voxel of the computational grid. Using Equation (1) the synthetic FBE was then computed for each band, and using Equation (4) the score R was

computed at each tomographic voxel. As an example, Figure 2 shows Carrington maps of the score R for both rotations at the two sampled heights. Black regions correspond to non-reconstructed voxels, and the thick-black curves indicate the open/closed boundaries in the PFSS model.

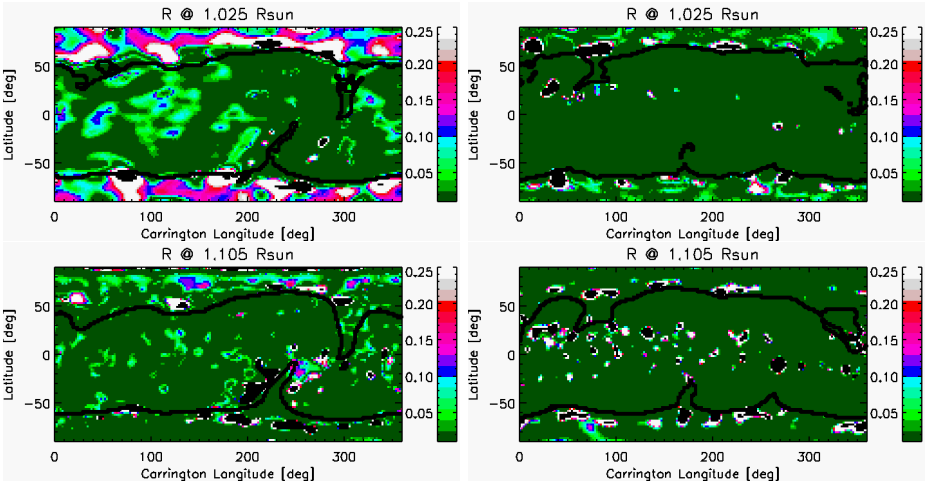

Figure 2. Carrington maps of the score R (see text) for CR-1915 (left panels) and CR-2081 (right panels). Top and bottom panels show the results at two sample heliocentric heights, 1.025 and 1.105 $R_\odot$, respectively. As in Figure 1, black regions correspond to non-reconstructed voxels and thick black curves indicate the open/closed boundaries in the PFSS model.

In the case of CR-2081 the vast majority of the coronal volume is characterized by $R < 0.01$, which means that the LDEM is able to reproduce the tomographic emissivities within a 1% accuracy. The same happens in the closed region of CR-1915, where there are some regions with somewhat larger values, but still $R < 0.05$ mostly everywhere. The open region of CR-1915, on the other hand, exhibits larger values of the score R. Voxels for which the parametric LDEM achieves a score $R > 0.1$ are excluded of the statistical analysis that follows. In the case of EIT-based reconstructions those voxels are more common in open regions, specially at low heights and in the northern hemisphere, most probably due to specific contamination issues seen in EIT 284 Å images around the northern pole.

3.2. 3D Density and Temperature

Once the LDEM was determined for each rotation, the electron density N_e and electron mean temperature T_m were computed at each voxel of the tomographic computational grid by means of Equations (2) and (3). As an example, Figures 3 and 4 show the results for both rotations at the same two sampled heights of Figure 1. Black voxels correspond to non-reconstructed regions, as discussed in the previous Section.

While CR-2081 was highly axisymmetric and showed virtually no ARs (except for a very small one around latitude +30° and longitude 50°, CR-1915 showed a

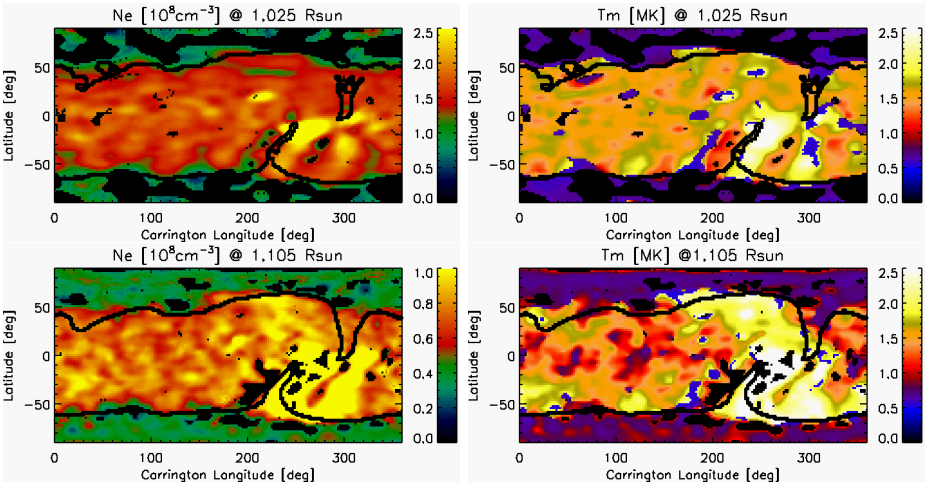

Figure 3. Carrington maps of N_e (left panels) and T_m (right panels) for CR-1915. Top and bottom panels show the results at two sample heliocentric heights, 1.025 and 1.105 $R_\odot$, respectively. Black voxels correspond to non-reconstructed regions (see text) and thick black curves indicate the open/closed boundaries based on the PFSS model.

very large AR in the Southern hemisphere, NOAA 7986, centered around latitude $-30°$ and longitude 280°. Note that, except for this large AR, in both rotations the open-closed boundaries derived from the respective PFSS model closely match the shape of contour levels of the tomographic maps of both the electron density and the electron mean temperature. Closed regions are characterized by relatively larger values of density and temperature in comparison to the nearby open regions. This is not the case around the large AR in CR-1915, which was surrounded by equatorial extensions of both the southern and northern CHs as seen in the EUV images, features that are reproduced by the PFSS model. In that region, the lack of match between the open-closed boundaries and the tomographic reconstructions of density and temperature is evident. This range of longitudes is excluded from the analysis, as detailed below.

3.3. Tracing of DEMT Results

For both rotations, the DEMT 3D maps of electron density N_e and electron mean temperature T_m were traced along the magnetic field lines of their respective PFSS models, as described at the end of Section 2. In the case of closed loops, results were separated into their two legs, defined as the two segments that go from the coronal base up to the apex. For each open field line, and for each leg of the closed ones, an exponential fit was then applied to the $N_e(r)$ data points, and a linear fit applied to the $T_m(r)$ data points, as described by Equations (5) and (6) below, respectively,

$$N_e \;=\; N_0 \,\exp\left[\,-\,(h/\lambda_N)\;/\;(r/\mathrm{R}_\odot)\,\right], \tag{5}$$

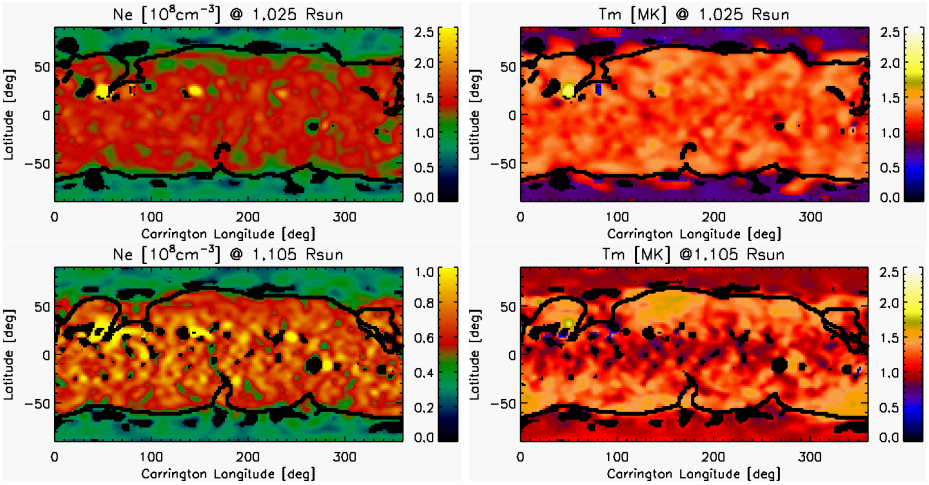

Figure 4. Same as Figure 3, but for CR-2081.

$$T_m \;=\; a\,r \;+\; b, \tag{6}$$

where $h \equiv r - 1\,\mathrm{R}_\odot$, and a and b are constants.

In the case of the electron density, the fitted function corresponds to the isothermal hydrostatic equilibrium solution, allowing for variation of the solar gravitational acceleration with height. After computing the footpoint ($r = 1.0\,\mathrm{R}_\odot$) electron density N_0 [cm^{-3}] and scale height λ_N [R$_\odot$], this choice of function provides a straightforward mean to directly evaluate how compatible is the observed coronal thermodynamical state with the hydrostatic solution, as analyzed in Section 4.2. In the case of the DEMT electron mean temperature, the linear fit allows characterization of its variation with height by means of a characteristic temperature gradient $a = dT_m/dr$ [MK/R$_\odot$] along each leg/loop.

As an explicit example, Figure 3.3 shows the electron density and electron mean temperature DEMT data points traced along the two legs of a sample small-closed field line of the PFSS model, and the corresponding fits.

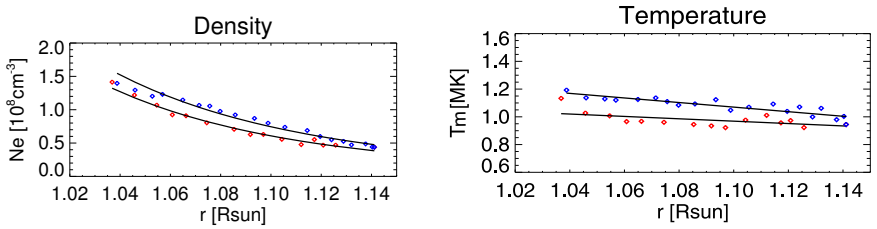

Figure 5. For a sample closed field line, the DEMT electron density (left panel) and electron mean temperature (right panel) data points (diamonds) are shown as a function of height. Blue and red diamonds correspond to different legs of the loop. The solid-black curves correspond to the functional fits given by Equations (5) and (6).

The quiescent closed corona and open regions studied by DEMT are characterized by electron density scale heights of order $\lambda_N \lesssim 0.1\,\mathrm{R}_\odot$ (see Table 2). This implies that the electron density data points exhibit a noticeable variation over the height range of DEMT analysis. For a given leg/loop, a good measure of how the quality of the exponential fit to the electron density data is then given by the coefficient of determination $r^2 \equiv 1 - S_{\rm res}/S_{\rm tot}$, where $S_{\rm res}$ is the sum of the squared residuals and $S_{\rm tot}$ is the sum of data's deviations from the mean.

In the case of the electron mean temperature T_m, its variability over the DEMT range of heights is much smaller compared to the electron density. The coefficient of determination of the linear fit can then be nearly zero for excellent fits when the temperature gradient is weak enough. Measuring the quality of the linear fit to the temperature based on the coefficient of determination, as previously done in papers I and II, would only select strong enough gradients. Interested in expanding the analysis to weak temperature gradients (i.e., quasi-isothermal structures), the criterion has been upgraded to a new one in the present study. Based on the estimation of the systematic errors of the DEMT technique propagated into the electron temperature, detailed in Section 3.6 below, the linear fit is required to match the data points within the error bars for a majority of them. Also, while in papers I and II the linear fit to the temperature data points was implemented by means of the least-squares method, in this work the Theil-Sen estimator was used. This method is more robust to outliers, which has proven to significantly increase the sample size over previous analysis. Outliers are common in SRT results, mainly due to the effect of unresolved coronal dynamics on the assumed static solution of the global optimization problem.

As in papers I and II, the statistical analysis of the results is based only on those field lines for which the traced DEMT results can be fairly described by the exponential and linear fits to the electron density and the electron mean temperature data points, respectively. The field line selection criteria enumerated below (also upgraded respect to previous works) are based on experimentation with the actual data sets, aiming at maximizing the data sample size. As a result, the selected loops evenly sample the DEMT results through the coronal volume covered by the technique, and constitute a fair representation of the complete results. To be selected a loop must meet all following conditions,

i) Each leg of the loop must go through at least five tomographic grid cells with reconstructed data, and there must be at least one data point in each third of the range of heights spanned by the loop.
ii) The coefficient of determination of the exponential fit to the density is $r^2 > 0.75$ in each leg of the loop.
iii) The linear fit to the temperature matches the DEMT values within their estimated error for at least a fraction $F = 0.75$ (i.e. 75%) of the data points in each leg of the loop.

In the following sections we show in detail the statistical results for all field lines meeting these criteria.

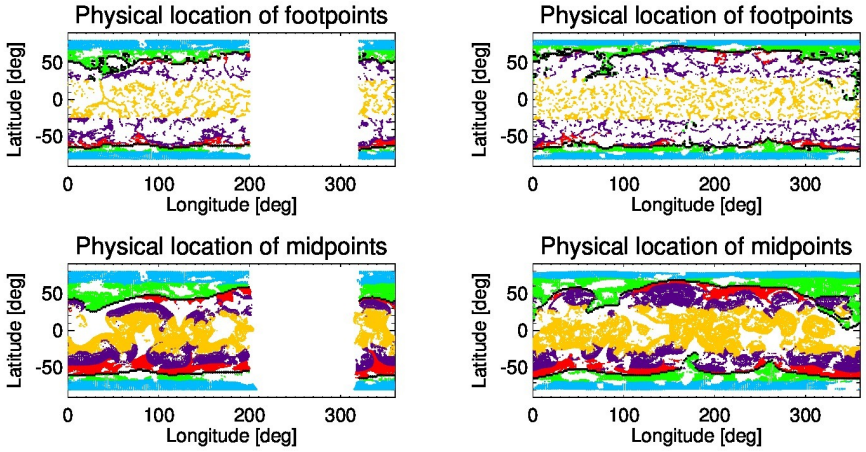

Figure 6. Latitude-longitude location of field lines meeting the criteria listed in Section 3.3, at heights $1.0\,R_\odot$ (footpoints, top panels) and $1.105\,R_\odot$ (midpoints, bottom panels), for CR-1915 (left panels) and CR-2081 (right panels). In the case of CR-1915 the region affected by the presence of a large AR is excluded of the analysis. Different colors identify diverse thermodynamical and magnetic structures, as described in the text and summarized in Table 1. In all panels the thick black curves indicate the boundary between the magnetically open and closed field lines, according to the PFSS model.

3.4. Coronal Regions

For the two analyzed rotations, Figure 6 shows the latitudinal-longitudinal location of all field lines that meet the criteria listed in Section 3.3, at two heights, namely $1.0\,R_\odot$ (footpoint) and $1.105\,R_\odot$ (dubbed "midpoint" hereafter, the middle point within the tomographic computational ball). In the case of CR-1915, field lines with footpoint in the longitude range $[200°, 320°]$ were excluded of the analysis, as they are within and around the region affected by the presence of the large AR. In these maps, locations are indicated with five different colors to label diverse coronal regions that were discriminated as explained next.

Visual inspection of the DEMT results for CR-2081 in Figure 4 reveals two clearly distinct thermodynamical states within the equatorial streamer belt (closed field lines). At the middle height of the tomographic grid ($1.105\,R_\odot$) "low-latitudes", roughly in the range $[-30°, +30°]$, exhibit lower temperatures than "mid-latitudes" (outside that range but still in the closed region). This is a stable pattern observed in all rotations analyzed during the SC 23/24 minimum in Paper II (see their Figure 6). The same is observed for CR-1915 outside the longitude range dominated by the AR, although it is not so evident visually in Figure 3 due to the scale in the graph, selected to be able to reflect the AR temperature.

To highlight this pattern, Figure 7 shows for both rotations the latitudinal variation of both the electron density and the electron mean temperature at the height $r = 1.105\,R_\odot$, averaged over all longitudes (excluding the AR in the case of CR-1915). While the temperature shows a maximum in each hemisphere,

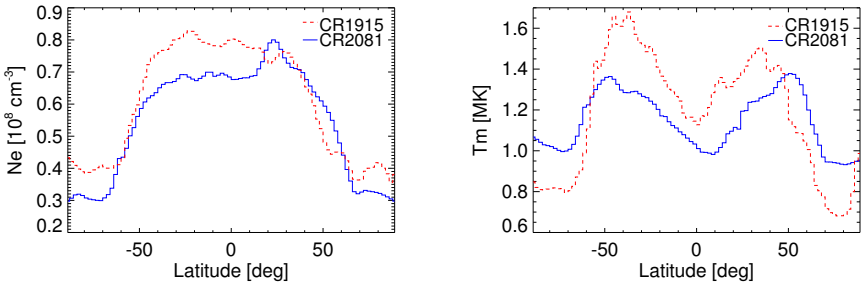

Figure 7. Latitudinal variation, in both rotations, of the tomographic electron density (left) and electron mean temperature (right) at height $1.105\,R_\odot$, averaged over all longitudes (excluding the AR in the case of CR-1915).

the density has a simpler behavior, with higher values in the low-latitudes of the streamer and a nearly monotonic decrease towards larger latitudes. A similar plot at the lowest height of the tomographic computational ball ($1.025\,R_\odot$) shows a much weaker dependence with latitude within the streamer belt.

Based on those thermodynamical characteristics, the analyzed coronal volume was dissected in different regions of analysis to be compared between both periods. For both rotations, in Figure 7 the latitude at which the temperature reaches the average value between the (nearly) equatorial minimum and the mid-latitude maximum was determined, for both hemispheres. Those two latitudes, found at height $r = 1.105\,R_\odot$, were then traced down to height $r = 1.0\,R_\odot$ based on the mean expansion factor of the open-closed boundary between the two heights. The two resulting values define the northern and southern longitude-averaged footpoint of the latitudinal boundary between the hotter mid-latitudes and the cooler low-latitudes within the equatorial streamer.

Based on those results, the closed magnetic field lines of the PFSS model (that we will identify as the equatorial streamer region in this work) were then discriminated between those with footpoint at low-latitudes and those with footpoint at mid-latitudes. Field lines in the mid-latitudes were further discriminated between those being small, which are in general structures with both footpoints in the same hemisphere, and those being large, being mostly trans-equatorial structures shaping the outer boundary of the closed field lines of the streamer belt. As a result, closed field lines were divided in the three different groups: low-latitudinal, mid-latitudinal, and streamer-boundaries, indicated in Figure 6 with yellow, violet, and red colors, respectively. Table 1 summarizes these regions and their acronyms in both hemispheres.

The open field regions (that we will identify as the CHs in this work) were divided in two subregions, low and high latitudes, thought to be respectively associated to the slow and fast components of the solar wind (Vásquez, van Ballegooijen, and Raymond, 2003; Nerney and Suess, 2005; Oran *et al.*, 2015). To that end, in each hemisphere, the longitude-averaged middle latitude θ_m between the open-closed boundary and latitude $\pm 80°$ was determined at $r = 1.0\,R_\odot$. We note that at higher latitudes tomographic reconstruction are more affected by

stray light contamination in CHs, and also the PFSS model is computed up to latitude is ±84° (Tóth, van der Holst, and Huang, 2011). Accordingly, in each hemisphere the open field lines in Figure 6 were then discriminated between those with footpoint at latitudes lower and higher than $\theta_{\rm m}$, indicated in Figure 6 with cyan and green colors, respectively.

Table 1. Classification and acronym of diverse coronal regions, and color code in Figure 6.

Coronal Structure	Region	Acronym	Loop Class	Color Code
North Coronal Hole	High Latitudes	CH-Nh	Open	Cyan
	Low Latitudes	CH-Nl	Open	Green
Equatorial Streamer	North Boundary	ES-Nb	Closed Large	Red
	North Mid Latitudes	ES-Nm	Closed Small	Violet
	Low Latitudes	ES-Ll	Closed Small	Yellow
	South Mid Latitudes	ES-Sm	Closed Small	Violet
	South Boundary	ES-Sb	Closed Large	Red
South Coronal Hole	Low Latitudes	CH-Sl	Open	Green
	High Latitudes	CH-Sh	Open	Cyan

3.5. Comparative Statistical Analysis of The Two Rotations

For both rotations, all field lines that meet the criteria listed in Section 3.3 were separated into the coronal regions described in Section 3.4 and summarized in Table 1. For each field line, the data points of electron density and electron mean temperature versus height were fitted to the functions given by Equations (5) and (6) of Section 3.3. As a result, the footpoint electron density N_0 and scale height λ_N were computed for each field line, as well as the temperature gradient $a = dT_m/dr$, and the height-averaged (along the loop) electron mean temperature $\langle T_m \rangle$. As the DEMT technique studies only coronal conditions, i.e. above height $r \approx 1.025\,{\rm R}_\odot$, the exponential fit to the electron density data versus height was used to compute the coronal base electron density here defined as $N_{\rm CB} \equiv N_e(r = 1.025\,{\rm R}_\odot)$. Also, for each field line the coronal base magnetic field strength $B_{\rm CB} \equiv B(r = 1.025\,{\rm R}_\odot)$ and its height-averaged value along the loop $\langle B \rangle$ were also computed.

As way of example, Figure 8 shows the statistical results of both rotations for all field lines traced in the low-latitudes of the equatorial streamer (region ES-Ll, left panels) and the the southern equatorial streamer mid-latitudes (region ES-Sm, right panels). From top to bottom the panels show the statistical distribution of $N_{\rm CB}$, λ_N, $\langle T_m \rangle$ and $B_{\rm CB}$. In each panel the median m, mean μ, fractional standard deviation σ/μ, and number of traced loops N, are indicated. In a similar fashion, Figure 9 shows the corresponding results for the southern CH low-latitudes (region CH-Sl, left panels) and the southern CH high-latitudes (region CH-Sh, right panels).

For all coronal regions in both rotations, Table 2 summarizes the median value (indicated as "Md") of the statistical distribution of each physical quantity

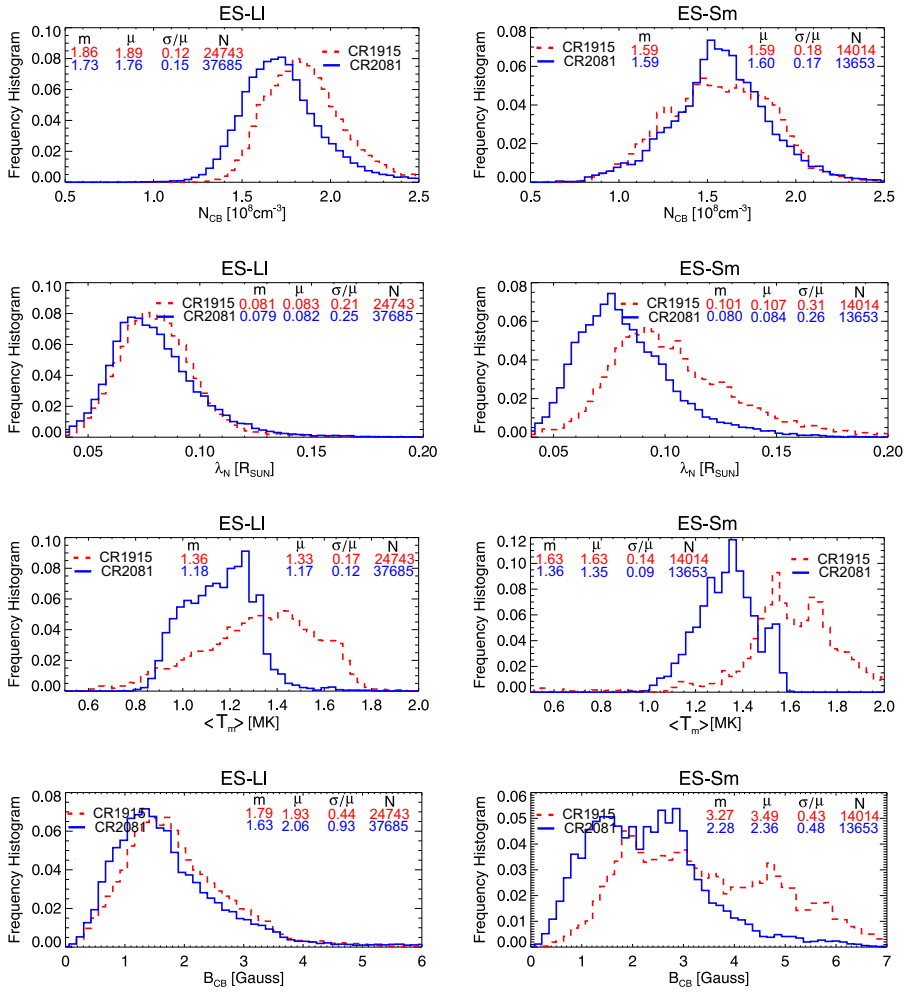

Figure 8. Comparative statistical distributions of (from top to bottom): the coronal base electron density $N_{\rm CB} \equiv N_e(r = 1.025\,{\rm R}_\odot)$, the electron density scale height λ_N, the average electron mean temperature $\langle T_m \rangle$, and the coronal base magnetic field strength $B_{\rm CB}$, along all field lines traced in the low-latitudes of the equatorial streamer (region ES-Ll, left panels) and the southern mid-latitudes of the equatorial streamer (region ES-Sm, right panels), for CR-2081 (solid-blue) and CR-1915 (dashed-red). In each panel the median m, mean μ, fractional standard deviation σ/μ, and number of traced loops N, are indicated.

derived from the analysis. For CR-2081 quantities are expressed as absolute values, while for CR-1915 they are informed relative to the corresponding result for CR-2081. As an example, the median value of $N_{\rm CB}\,[10^8\,{\rm cm}^{-3}]$ for the ES-Ll region during CR-2081 is ≈ 1.73, while it is $\approx 7.6\%$ higher for the same region during CR-1915, i.e. $\approx 1.86 = 1.73\,(1 + 0.076)$. In a similar fashion, Table 3 summarizes the standard deviation (indicated as "SD") of the statistical

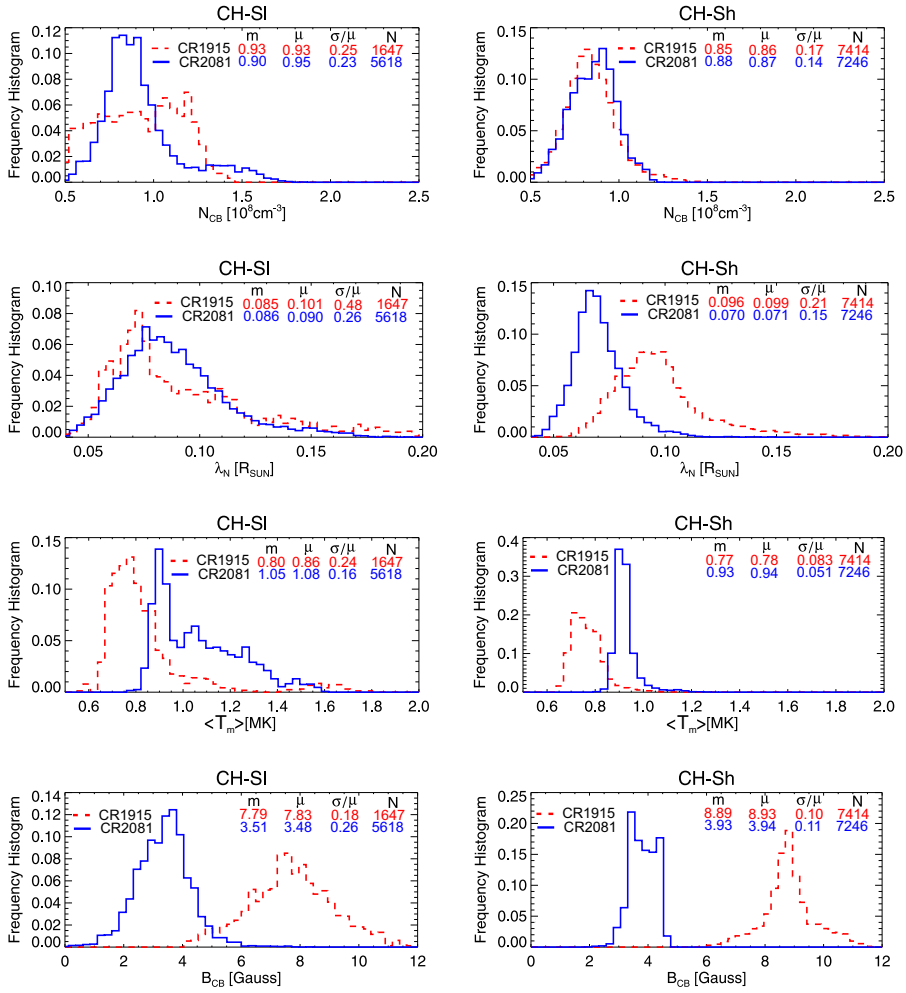

Figure 9. Same as Figure 8 but for all field lines traced in the low-latitudes of the southern coronal hole (region CH-Sl, left panels) and the high-latitudes of the southern coronal hole (region CH-Sh, right panels).

distribution of each physical quantity derived from the analysis (as a function of their mean value, indicated as "Mn").

Tables 2 and 3 summarize thus the quantitative comparative analysis between the results of the two target rotations sampling both minima. The following major results concerning the structure of each rotation individually and their comparison can be drawn.

Table 2 indicates that for CR-2081 the values of all physical quantities exhibit a strong symmetry between the northern and southern (N and S) hemispheres. Within its equatorial streamer, increasing latitudes show decreasing coronal base

Table 2. Median value (indicated as "Md") of the statistical distribution of $N_{\rm CB}$, λ_N, and $\langle T_m \rangle$ in each coronal region defined in Table 1. For CR-2081 values are expressed in absolute terms, while for CR-1915 they are informed as a percentual variation relative to the CR-2081 value.

Region	Md($N_{\rm CB}$) [10^8 cm^{-3}]	Md(λ_N) [10^{-2} R$_\odot$]	Md($\langle T_m \rangle$) [MK]	$B_{\rm CB}$ [G]
CH-Nh	0.94 (-11.4%)	7.0 (+34.3%)	0.91 (-20.6%)	3.80 (+49.2%)
CH-Nl	1.05 (- 4.5%)	8.0 (+25.0%)	1.06 (- 3.9%)	3.23 (+27.0%)
ES-Nb	1.33 (+11.8%)	9.4 (+ 4.2%)	1.33 (+ 8.3%)	3.33 (-0.04%)
ES-Nm	1.58 (+ 4.7%)	8.4 (- 2.4%)	1.37 (+ 6.2%)	2.33 (+0.05%)
ES-Ll	1.73 (+ 7.6%)	7.8 (+ 3.8%)	1.18 (+15.0%)	1.63 (+10.2%)
ES-Sm	1.59 (+ 0.1%)	8.0 (+25.0%)	1.36 (+20.2%)	2.33 (+43.6%)
ES-Sb	1.24 (- 6.7%)	9.3 (+26.9%)	1.38 (+16.9%)	2.93 (+80.7%)
CH-Sl	0.90 (+ 3.8%)	8.6 (- 1.1%)	1.05 (-23.2%)	3.51(+121.9%)
CH-Sh	0.88 (- 3.4%)	7.0 (+37.1%)	0.93 (-17.0%)	3.93(+126.5%)

density, and increasing density scale height, electron temperature and magnetic field strength. The equatorial streamer in CR-1915 shows a much more complex structure and a clear N/S asymmetry, with its northern hemisphere exhibiting somewhat larger basal density than its southern one, as well as considerably smaller density scale height, electron temperature and magnetic field strength. In both rotations the CH regions are characterized sub-MK temperatures, and coronal base densities of order $\approx 1/2$ of the equatorial streamer low-latitudes. The open regions of the CHs also show a strong N/S symmetry in CR-2081 for all quantities, and asymmetry for CR-1915.

A comparison of the results between the two rotations within the equatorial streamer belt shows that CR-1915 is characterized by larger values of both electron density and temperature compared to CR-2081. In the coronal hole regions, CR-1915 exhibits systematically lower temperatures compared to CR-2081, as well as larger values of the density scale height. To establish if the differences in the results between the two rotations are significant, the next Section 3.6 estimates its error bars due the dominating systematic uncertainties.

Also, within the streamer belt the magnetic field strength is similar in both rotations in the northern hemisphere, while in the southern hemisphere CR-1915 exhibits $10-80\%$ larger values compared to CR-2081, with increasing difference for larger latitudes. In the coronal holes, the magnetic field strength of CR-1915 is much larger than for CR-2081, exhibiting values up to 50% larger in the northern hemisphere and more than twice larger in the southern hemisphere.

Table 3 informs the standard deviation of the different physical quantities in terms of their mean values in each region. This dimensionless ratio is a measure of the coronal variability of a given quantity in each region. For CR-2081, the equatorial streamer is characterized by a quite uniform variability for all thermodynamical quantities, being in average of order $\approx 18\%$ for the coronal base density $N_{\rm CB}$, $\approx 26\%$ for the density scale height λ_N, and $\approx 9\%$ for the mean

Table 3. Same as Table 2 but for the standard deviation (indicated as "SD") of the statistical distribution of $N_{\rm CB}$, λ_N, and $\langle T_m \rangle$, relative to the mean value (indicated as "Mn"), in each coronal region.

Region	$\frac{\rm SD(N_{CB})}{\rm Mn(N_{CB})}$	$\frac{\rm SD(\lambda_N)}{\rm Mn(\lambda_N)}$	$\frac{\rm SD(\langle T_m \rangle)}{\rm Mn(\langle T_m \rangle)}$	$\frac{\rm SD(B_{CB})}{\rm Mn(B_{CB})}$
CH-NH	0.11 (+70%)	0.13 (+74%)	0.03 (+681%)	0.20 (-33%)
CH-Nl	0.29 (- 0%)	0.28 (+ 6%)	0.17 (+120%)	0.46 (-15%)
ES-Nb	0.19 (-39%)	0.23 (- 7%)	0.07 (+149%)	0.19 (-39%)
ES-Nm	0.17 (- 8%)	0.29 (-10%)	0.10 (+ 54%)	0.48 (-27%)
ES-Ll	0.16 (-19%)	0.25 (-15%)	0.12 (+ 46%)	0.93 (-52%)
ES-Sm	0.18 (+ 5%)	0.27 (+17%)	0.09 (+ 56%)	0.48 (-10%)
ES-Sb	0.18 (+37%)	0.24 (+45%)	0.09 (+131%)	0.35 (+24%)
CH-Sl	0.23 (+11%)	0.26 (+85%)	0.16 (+ 47%)	0.26 (-30%)
CH-Sh	0.15 (+15%)	0.16 (+36%)	0.05 (+ 63%)	0.11 (- 1%)

electron density $\langle T_m \rangle$. Comparatively, the streamer region of CR-1915 shows a less uniform variability for the electron density at the coronal base and the scale height, being in places higher or lower than for CR-2081, although with values of similar order. The electron temperature on the other hand shows in CR-1915 a systematically and considerably larger variability than in CR-2081. The magnetic field strength variability shows much less uniform values in both rotations, systematically increasing with decreasing latitude for the streamer belt in both rotations, which is expected as the mean field strength weakens towards the equator.

In the open regions of the CHs it is interesting to note that the variability of all quantities is systematically larger in the low-latitudes compared to the high-latitudes, typically by a multiplicative factor of $\approx 2-3$. This is consistent with the more intermittent characteristic of the slow component of the solar wind, usually associated to the lower latitudes of the open region. In the case of thermodynamical quantities, this factor could be partly due to the fact that in the low-latitudes of the open region DEMT data can be "contaminated" by typical values of the closed region. In any case, the same table reveals a much less uniform variability of the same quantities for CR-1915, as well a considerably and systematically much larger variability of the electron temperature in all regions. In particular, in the high latitudes of the northern hemisphere, the extremely large variability is most probably an artifact due to stray light contamination in the EIT data.

3.6. Systematic Uncertainties in DEMT Results

The dominant sources of systematic uncertainty in DEMT are the radiometric calibration of the EUV images, and the determination of the tomographic regularization level (Frazin, Vásquez, and Kamalabadi, 2009; Vásquez, Frazin, and Kamalabadi, 2009; Vásquez, Frazin, and Manchester, 2010; Vásquez *et al.*, 2011). Huang *et al.* (2012) analyzed for the first time the impact of the former

in the case of EUVI data, while Nuevo *et al.* (2015) originally treated both sources simultaneously using data taken by the Atmospheric Imaging Assembly (AIA) instrument, on board the Solar Dynamics Observatory (SDO) mission. Their approach is adapted here for the purpose of analyzing both EUVI and EIT data. The procedure is fully described in Appendix A, where the results are detailed in Tables 7 and 8. Next, the main results are highlighted.

For each thermodynamical quantity in Table 2, the uncertainty propagation analysis in the Appendix details their mean value μ and uncertainty σ, in each coronal-subregion. For a given thermodynamical quantity in a specific coronal region, let us name now the values obtained for both rotations μ_a and μ_b, labeling as a the lower value, i.e. so that $\mu_a < \mu_b$ (note that in some cases μ_a corresponds to CR-1915, while in others to CR-2081). Their respective uncertainties are correspondingly named σ_a and σ_b. The absolute overlap S and percent relative overlap S_r between both results are next defined as,

$$S \equiv (\mu_a + \sigma_a) - (\mu_b - \sigma_b), \tag{7}$$

$$S_r \equiv 100\,\frac{S}{\mu_b - \mu_a}. \tag{8}$$

Note that, for each thermodynamical quantity in a given coronal region, if $S_r < 0$ the difference between both results exceeds their uncertainty, while if $S_r > 0$ there is an overlap between both results. In this latter case, it is important to note that very large overlap values ($S_r > 100\%$) correspond to cases in which $\mu_b - \mu_a$ is very low, i.e. cases in which very similar results where obtained for both rotations.

Table 4. Percent overlap measure S_r (see text) between the result for both rotations of the quantities $N_{\rm CB}$, λ_N, and $\langle T_m \rangle$ in each coronal region.

Region	$N_{\rm CB}$	λ_N	$\langle T_m \rangle$
CH-NH	- 45	- 86	- 70
CH-Nl	+ 32	- 82	+1004
ES-Nb	- 24	+ 30	+ 91
ES-Nm	+ 29	+157	+ 147
ES-Ll	- 41	- 4	+ 58
ES-Sm	+679	- 87	- 60
ES-Sb	+188	- 77	- 52
CH-Sl	+413	+651	- 57
CH-Sh	+110	-130	- 62

In the low-latitudes of the equatorial streamer, there is no overlap of the CR-1915 and CR-2081 results for both the coronal base density and the density scale

height, while there is overlap between the results for temperature. In the southern hemisphere of the equatorial streamer there is no overlap for the temperature results, nor for the density scale height, while the very high overlap of the basal densities is due to their differences being minimal (as seen for example in the top-right panel of Figure 8). In the northern hemisphere of the equatorial streamer belt most of the results overlap. In the southern CH temperature results do not overlap, while density results do. Given that the EIT images show a strong contamination in the northern coronal hole we skip the comparative analysis of results in that region.

Combining the comparative information of Table 2 with the error bar analysis in Table 4 we summarize next where differences of results between the two rotations are significant (larger than the uncertainty level) and where the two results are similar (i.e. the difference is within the uncertainty level). In the low latitudes range of the streamer belt CR-1915 exhibits $\approx 8\%$ larger densities than CR-2081, while differences in temperature between the two rotations are within the uncertainty levels. In the southern hemisphere of the streamer belt CR-1915 exhibits $\approx$ 20% larger temperatures than CR-2081, as well as $\approx$ 25% larger electron density scale heights (in that region the very large overlap in coronal base electron densities is due their values being very similar). In the northern hemisphere of the streamer belt the electron temperature and density of both rotations do not differ significantly. Concerning the southern CH, while differences in density between both rotations are not significant, CR-1915 exhibits $\approx 20\%$ lower temperatures than CR-2081.

EUV images are also affected by instrumental stray light contamination, which can be corrected by deconvolution of the point spread function (PSF). While in the case of EIT there is no reliable determination of its PSF, it has been well determined for EUVI by Shearer *et al.* (2012). To estimate the impact of its deconvolution in DEMT studies, the analysis of Section 3.5 was repeated for CR-2081 using stray light uncontaminated EUVI images. The details of that study is the subject of a separate publication (Lloveras *et al.*, 2017). The main effect of the stray light removal is a systematic increase of the coronal base electron density by 7 to 15%, and a systematic decrease of the electron density scale height by 5 to 10%, depending on the coronal region. This is consistent with the main effect of the PSF-deconvolution on the images being to increase the contrast level, which increases both the brightness near the limb and the radial gradient of the image intensity. On the other hand, the effect of the stray light removal in temperature determinations is found to be unsystematic and much less important (less than 1%). This is a result of PSF-deconvolution affecting all bands by similar correction factors, which does not alter the shape of the resulting LDEM (upon which temperature determination depends) but only its area (upon which only density determinations depend). EIT results are likely affected in a similar systematic fashion and by comparable factors, so that the comparative analysis above is possibly not to be affected by stray light removal.

4. Results: Temperature Structures

The gradient of the electron temperature with height derived from combining the DEMT and PFSS techniques was first analyzed by Huang *et al.* (2012) for CR-2077 during the SC 23/24 minimum. While loops at mid-latitudes were found to mainly have positive radial gradients, i.e. $dT_m/dr > 0$ (loops dubbed as "up"), those at low-latitudes where found to be dominated by structures with gradients of the opposite sign (loops dubbed as "down"). Later on, Nuevo *et al.* (2013) studied the evolution of up and down loops for several CRs with different levels of global activity selected around the SC 23/24 minimum. They found the down loops to always be mainly confined to low-latitudes, and their population size was found to be anti-correlated with the level of activity of the solar corona.

From a physical point of view, the reason for the existence of down and up loops lies in the scale height of the heating mechanisms. Down loops can be expected if heating mechanisms are strongly confined to the footpoints (Serio *et al.*, 1981; Aschwanden and Schrijver, 2002), while up loops are due to the heating being more uniformly distributed along it. Studying these structures provides then useful constraints for coronal heating models. Nuevo *et al.* (2013) speculated a physical scenario in which Alfvén waves are efficiently converted to compressive modes in down loops with $\beta \sim 1$ (which favors the mode conversion) and then quickly damped at lower heights, while in up loops with $\beta < 1$, the damping occurs by reflection of Alfvén waves and turbulent cascade more uniformly along the magnetic structure.

Motivated by the two aforementioned DEMT + PFSS studies, Schiff and Cranmer (2016) recently developed steady-state models of large-scale coronal structures, similar to those studied by DEMT. In an attempt to reproduce stable long-lived up and down loops, they consider time-averaged heating rates in their models, consistent with the DEMT low time resolution. In their study they consider heating via MHD turbulence cascade, and treat also the transfer of energy between Afvén and compressible waves. As a result, their models reproduce both up and down loops, as well as isothermal structures, depending on the values of different relevant physical parameters.

In this section, a comparative analysis of up/down structures, as well as quasi-isothermal (dubbed "QI" hereafter) structures, for both analyzed rotations is included. In the context of this study, a coronal magnetic loop can be regarded as QI in the coronal region studied by the technique if the temperature gradient is weak enough, within the uncertainties involved, compared to the range of coronal heights δr spanned by the loop. More specifically, $\delta r = r_{\rm max} - r_{\rm base}$, where $r_{\rm base} = 1.025\,{\rm R}_\odot$, and $r_{\rm max} = r_{\rm appex}$ for small loops, or $r_{\rm max} = 1.2\,R_\odot$ (the maximum height of the tomographic computational ball) for large loops.

A loop is then classified as QI if $|dT_m/dr| \lesssim \Delta(T)\,/\,\delta r$, where dT_m/dr is the temperature gradient of the linear fit to the temperature data points, and $\Delta(T)$ is the characteristic uncertainty in temperature data points due to the systematic errors discussed in Section 3.6. The uncertainty propagation analysis (detailed in Appendix A) gives as a result characteristic values of the uncertainty of individual temperature data points of order $\Delta(T) \approx 0.06\,{\rm MK}$ and $\Delta(T) \approx 0.13\,{\rm MK}$ for CR-1915 and CR-2081, respectively, with some variability (of order

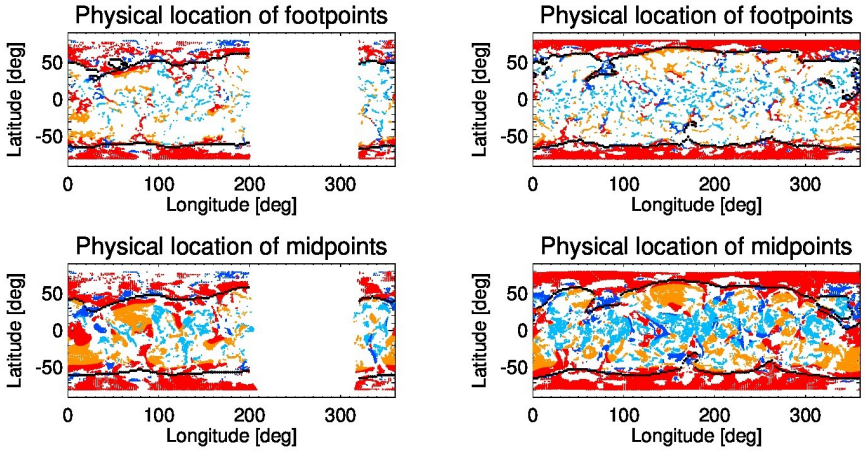

Figure 10. Latitude-longitude location of up loops (in orange/red colors for small/large structures) and down loops (in cyan/blue colors for small/large structures), at heights 1.0 $R_\odot$ (footpoints, top panels) and 1.105 $R_\odot$ (midpoints, bottom panels), for CR-1915 (left panels) and CR-2081 (right panels). In all panels the thick black curves indicate the boundary between the magnetically open and closed field lines, according to the PFSS model.

10%) depending on the coronal region. As a consequence, the characteristic temperature uncertainty for CR-1915 is ≈ 2 times larger that of CR-2081. The rest of the loops, for which $|dT_m/dr| > \Delta(T) \,/\, \delta r$, are further classified into the up and down classes, upon the sign of the temperature gradient being positive or negative, respectively.

This procedure, being more sophisticated than that used in the studies by Huang *et al.* (2012), and Nuevo *et al.* (2013), allows inclusion of QI structures which are also of interest to characterize the thermodynamical state of the solar corona. This classification criterion was applied to all loops selected and analyzed in Section 3, and results for the up/down and QI loops are reported in Sections 4.1 and 4.2 below, respectively.

4.1. Up and Down Loops

Figure 10 shows the footpoint and midpoint location of both up and down loops for both CR-1915 and CR-2081. Down loops are indicated in cyan and blue for small and large structures, respectively. Up loops are indicated in orange and red for small and large structures, respectively. The midpoint map of up/down loops for CR-2081 (bottom-right panel) can be directly compared to the respective results of Nuevo *et al.* (2013) (see the middle-right panel of their Figure 6), to find that consistent results were obtained, with an increased sample size in this work, due to new selection/classification criteria here implemented. Most noticeably, within the streamer belt down loops dominate the low-latitudes and up loops middle latitudes, while open regions are fully dominated by up loops. The new most important single result of this section is that the analysis for CR-1915 reveals the presence of down loops also during the SC 22/23 minimum.

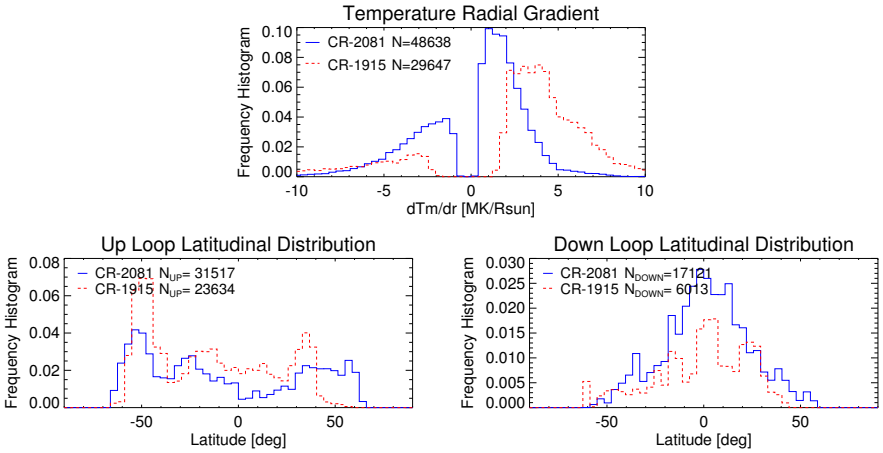

Figure 11. Statistical characteristics of the up and down loops of the magnetically closed region for CR-1915 (red-dashed lines) and CR-2081 (solid-blue lines). Top panel: histogram of the temperature radial gradient along each leg of the up and down loops. Bottom panels: histograms of the latitudinal distribution at $r = 1.105\,\mathrm{R}_\odot$ (midpoint) of the legs of the up (left panel) and down (right panel) loops. In each panel the total number N of legs is indicated, and each distribution is normalized to the sum of the number of up and down legs.

To compare the results in the magnetically closed region of both analyzed rotations, Figure 11 over-plots their respective histograms of temperature radial gradient (top panel), and their respective histograms of latitudinal distribution of the midpoint of the up loops (bottom left panel) and down loops (bottom right panel). The top panel shows that the temperature radial gradient characteristic values of CR-1915 are about twice those of CR-2081. Also, for both rotations, there is a missing population around $dT_m/dr \approx 0$ which corresponds to the QI loops (analyzed in the next section). Note that the QI missing population spans a rage of values of dT_m/dr for CR-1915 about twice as large that of CR-2081, consistently with their respective characteristic values of the temperature uncertainty $\Delta(T)$, detailed above. The bottom left panel shows that in both rotations the population of up loops peaks at middle latitudes and is lower around the equator. The bottom right panel shows that down loops are preferentially located around the equator for both rotations.

In analyzing several rotations around the SC 23/24 minimum, Nuevo *et al.* (2013) found that down loops were characterized by distinct values of the fundamental plasma parameter $\beta = p_{\mathrm{gas}}/p_{\mathrm{mag}} \approx 2N_e k_B T_e/(B^2/(8\pi))$, with N_e, T_e and B computed from the DEMT and PFSS models. They found down loops to be characterized by $\beta \gtrsim 1$, while up loops were characterized by $\beta < 1$. The importance of this relates to the physical mechanism they proposed as responsible for the existence of down loops, namely dissipation of Alfvén waves at very low heights in the corona, for which larger plasma β values are a necessary ingredient in the physical picture.

Figure 12 shows Carrington maps of the plasma β at the coronal base, and also at a mid height within the tomographic computational ball. It is readily

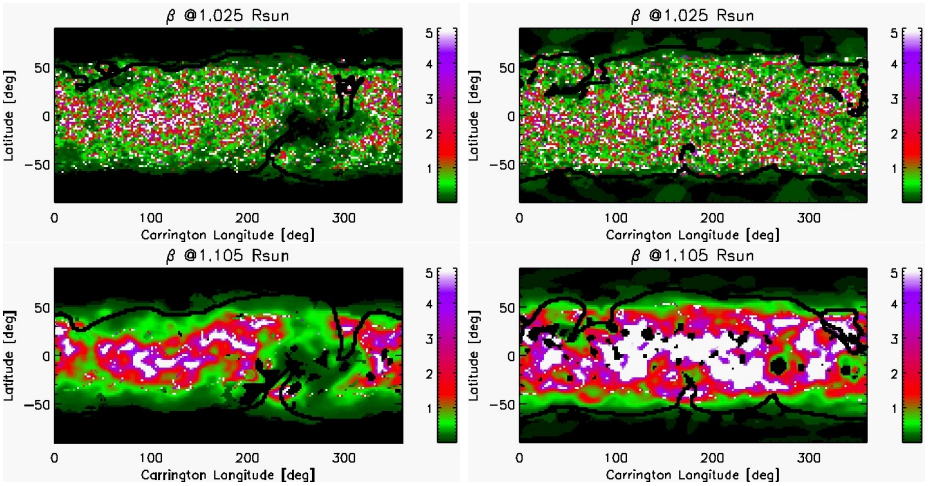

Figure 12. Carrington maps of β for CR-1915 (left panels) and for CR-2081 (right panels). Top and bottom panels show the results at 1.025 and 1.105 $R_\odot$ respectively.

seen that high beta values are observed in the lower latitudes (or "core") of the streamer belt, consistently with previous DEMT studies (Vásquez *et al.*, 2011; Nuevo *et al.*, 2013), other semi-empirical models (Li *et al.*, 1998; Gibson *et al.*, 1999; Vásquez, van Ballegooijen, and Raymond, 2003), as well as MHD models (Wang *et al.*, 1998; Suess, Wang, and Wu, 1996). In the case of CR-1915 the presence of the AR is evidenced by $\beta < 1$ in the whole region affected by it inside the streamer belt in the range of longitudes $\approx [220°, 320°]$.

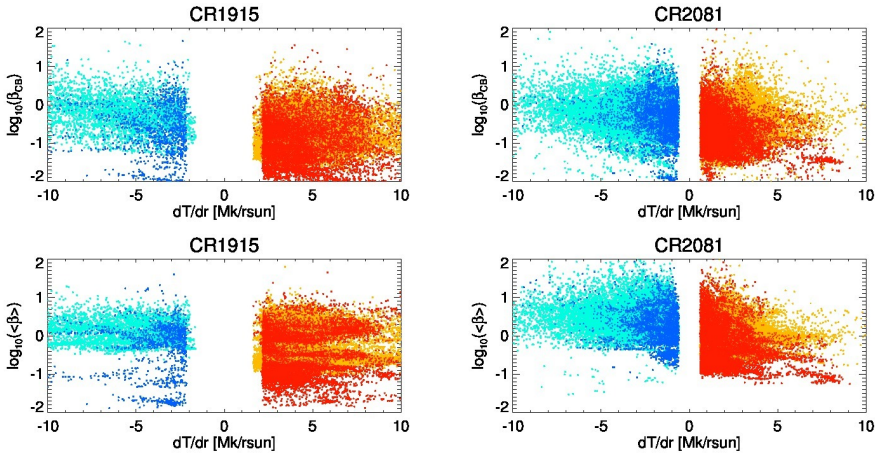

Figure 13. Scatter plots of the fitted temperature gradient dT_m/dr *vs.* β at the coronal base (top) and dT_m/dr vs. the mean value $\langle\beta\rangle$ (bottom), both in logarithmic scale. The panel from the left shows results from CR-1915 and the right shows CR-2081. In each panel up, down, small, and large structures are discriminated, using the same color code as in Figure 10.

To quantify the relationship between β and the different temperature structures, Figure 13 shows scatter plots of the temperature radial gradient dT_m/dr along each loop versus $\beta_{\rm CB}$ (at the coronal base) and also versus $\langle\beta\rangle$ (height-averaged along the loops). In each panel up, down, small, and large structures are discriminated using the same color code as in Figure 10. Table 5 summarizes the median β values for each type of structure. The Carrington maps and scatter plots of β, and the table with its statistics, can be directly compared to respective results by Nuevo *et al.* (2013). In the case of CR-2081 our results closely replicate theirs, but based on a larger sample size, while our results for CR-1915 are original and reveal similar trend. In both rotations we find down loops to be characterized by $\beta_{\rm CB} \sim 1$ and $\langle\beta\rangle \gtrsim 1$, while up loops are characterized by $\beta_{\rm CB} < 1$ and $\langle\beta\rangle \lesssim 1$.

Table 5. Median values of the β plasma parameter at the coronal base $\beta_{\rm CB}$ and height-averaged along each leg $\langle\beta\rangle$, discriminating their different types (up, down, QI, small and large) for both rotations.

	CR-1915		CR-2081	
Leg Type	Md($\beta_{\rm CB}$)	Md($\langle\beta\rangle$)	Md($\beta_{\rm CB}$)	Md($\langle\beta\rangle$)
Small Up	0.3	0.5	0.4	1.0
Small QI	0.5	0.9	0.7	1.9
Small Down	0.9	1.4	1.0	2.9
Large Up	0.2	0.3	0.2	0.5
Large QI	0.3	0.5	0.4	1.1
Large Down	0.4	0.8	0.8	1.6

4.2. Quasi Isothermal Loops

Figure 14 overplots the histograms of the temperature radial gradient of the QI loops (left panel), and of the latitudinal distribution of their midpoint (right panel). The left panel shows the population gaps missing in the up/down histogram in Figure 11, with CR-1915 exhibiting a wider span of temperature gradients due to its larger uncertainty in the temperature data points, as explained above in connection to the up/down loops. The right panel shows that in both rotations the population of QI loops distributes more uniformly in latitude than up/down for both rotations, showing a mild tendency to deplete near the equator. Consistent with QI loops having temperature radial gradient values intermediate to the up/down loops, Table 5 shows that, for each rotation and loop size, the median value of both $\beta_{\rm CB}$ and $\langle\beta\rangle$ are always intermediate to the respective up and down values.

For each leg of the QI loops, fit to the electron density data points, given by Equation (5), can be used to infer the electron temperature $T_{e,\rm fit}$ that is consistent with the density scale height λ_N, as given by the relationship $\lambda_N \approx 1.7\, k_B\, T_{e,\rm fit}\,/(m_p\, g_\odot)$, where $g_\odot$ is the Sun's surface gravitational acceleration,

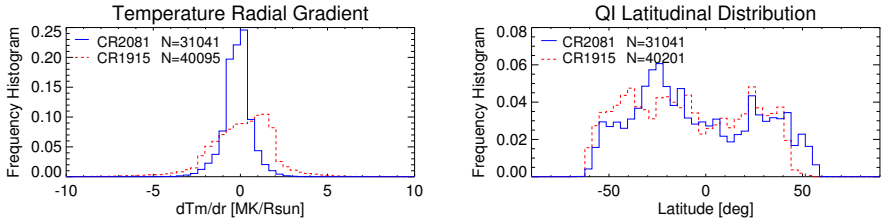

Figure 14. Statistical characteristics of the quasi isothermal loops for CR-1915 (red-dashed lines) and CR-2081 (solid-blue lines). Left panel: histograms of the temperature radial gradient along each leg of the QI loops. Right panel: histograms of the latitudinal distribution at $r = 1.105\,\mathrm{R}_\odot$ of the legs. In each panel the total number N of legs is indicated, and each distribution is normalized to the sum of the number of up and down legs.

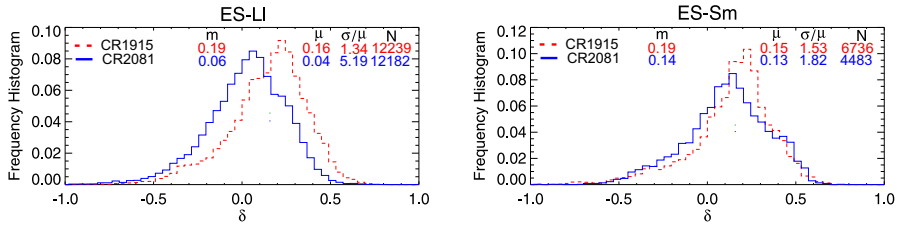

Figure 15. Histograms of δ in two regions of the equatorial streamer belt.

and the factor 1.7 accounts for the assumed $\approx 8\%$ helium abundance (Vásquez *et al.*, 2011). On the other hand, the average temperature along the loop $\langle T_m \rangle$ is the characteristic temperature of the QI legs. The relative difference between both temperatures can then be computed as

$$\delta \equiv \frac{\langle T_m \rangle - T_{e,\mathrm{fit}}}{\langle T_m \rangle}, \tag{9}$$

which is thus a dimensionless measure of the consistency between the tomographic result for a QI loop and the hydrostatic solution. A value $\delta \approx 0$ indicates a high consistency between the tomographic result and the hydrostatic regime, while larger values of $|\delta|$ indicate less consistency between them. As an example, Figure 4.2 shows the distribution of δ for all QI loops belonging to two selected coronal regions in both rotations, namely the low-latitudes and southern mid-latitudes of the equatorial streamer. Table 6 summarizes the statistics of δ for both rotations and all coronal regions.

In the case of the equatorial streamer during CR-2081, its low-latitudes and also its boundaries show histograms well centered near $\delta \approx 0$, with a larger systematic departure from that value in the mid-latitudes. It also shows a remarkable northern/southern symmetry, as with all previous results. In the case of the equatorial streamer during CR-1915, its values of δ show systematically larger departure from the null value. These results suggest thus that the streamer

core during CR-2081 was in a state quite consistent with the hydrostatic regime, while its mid-latitudes were less consistent with it. They also suggest the CR-1915 streamer thermodynamical status was overall less similar to the hydrostatic regime, which is consistent with a relatively more intermittent and active period.

Table 6. Median value (indicated as "Md") of the measure δ given by Equation (9), for quasi isothermal (QI) loops, and their sample size $N_{\rm QI}$ in each coronal region.

	CR-2081		CR-1915	
Region	Md(δ)	$N_{\rm QI}$	Md(δ)	$N_{\rm QI}$
CH-Nh	-0.01	11	-0.75	5974
CH-Nl	+0.01	1678	-0.59	2656
ES-Nb	+0.05	1023	+0.16	1351
ES-Nm	+0.14	3822	+0.24	2835
ES-Ll	+0.06	12182	+0.19	12239
ES-Sm	+0.14	4483	+0.19	6736
ES-Sb	+0.06	1599	+0.11	4898
CH-Sl	-0.07	537	-0.76	489
CH-Sh	-0.08	11	-0.92	3161

In the case of the CH regions, only CR-1915 shows a significant sample size of QI loops. This turns out to be due to the fact that temperature gradients are lower in these regions in the case of CR-1915 compared to CR-2081, which implies that more loops can be regarded as QI within the context of the analysis. Measured by the score δ, the CHs have the strongest lack of consistency with the hydrostatic regime, as expected for the open regions.

Finally, in both rotations, we note that the streamer regions are characterized by $\delta > 0$, while the CHs are characterized by $\delta < 0$. Departures of δ from the null value may be due to the presence of other pressure mechanisms. If so, the high goodness-of-fit measure r^2 suggests that such other processes must be linear in the plasma density. Another possibility is lack of isothermality among the different species, assumed in deriving the hydrostatic relationship between the density scale height and the electron temperature. Taking the tomographic temperature $\langle T_m \rangle$ as a measure o the "true" electron temperature, the proton temperature T_H can be expressed as (Vásquez *et al.*, 2011),

$$\frac{T_H}{\langle T_m \rangle} = \left(\frac{1+a}{2+3a} - \delta \right) \left(\frac{2+3a}{1+a\,T_{He}/T_H} \right) \simeq 1 - 2\,\delta, \tag{10}$$

where $a \approx 0.08$ is the coronal helium abundance respect to protons, and the last approximation assumes $T_{He} \approx T_H$ (it still holds to within $\approx 10\%$ if the two temperatures differ up to a factor of ≈ 2). This expression shows that the $\delta > 0$ values found in streamers may be due to electrons being hotter than protons, while the opposite may be happening in CH regions.

Lack of isothermality among species is a plausible regime in regions affected by more intermittent dynamics. The hotter mid-latitudes of the CR-2081 streamer, dominated by locally closed magnetic structures, may be an indication of a more dynamical scenario than in the core of the streamer. Lack of isothermality among species may also have been characteristic throughout the whole streamer during CR-1915, a rotation belonging to a more active and intermittent period. In CHs our results show $\delta < 0$ everywhere, with much higher absolute values for CR-1915. These results may indicate protons being hotter than electrons in those regions, with a much stronger departure for CR-1915 compared to CR-2081.

5. Discussion and Conclusions

In this work the combination of DEMT reconstructions and PFSS models has been used to perform a comparative study of the 3D thermodynamical state of the low solar corona ($1.02 - 1.23\,R_\odot$) for two rotations sampling the last two solar minima. Specifically the study compares rotations CR-1915 and CR-2081, respectively sampling the SC 22/23 and SC 23/24 minima. The SC 22/23 minimum was shorter, more active and intermittent. The SC 23/24 minimum was remarkably characterized by a ≈ 1 year period showing virtually no sunspots. Being CR-2081 near the end of that extremely quiet period, it was one of the most axisymmetric and quiet rotation on record from that period (Nuevo *et al.*, 2013).

Based on the observed thermodynamical properties of the results (Section 3.2) and the modeled magnetic structure (Section 3.3), the low solar corona was dissected in several regions for analysis (Section 3.4), as summarized in Table 1, which roughly correspond to different ranges of latitude. In both rotations 5 regions were identified within the equatorial streamer (ES, here defined as the magnetically closed region), and 2 regions were defined in both the northern and the southern polar CH (here defined as the magnetically open region of each hemisphere). Results of the analysis were compared between the corresponding regions in both rotations (Section 3.5), with their comparative statistics summarized in Tables 2 and 3. A propagation study of the systematic uncertainties of the DEMT technique on the thermodynamical results was performed (Appendix A), with its results summarized in Tables 7 and 8, discussed in Section 3.6, and their impact on how the thermodynamical results of both rotations overlap summarized in Table 4.

Next, we highlight conclusions from this analysis that are inherent to each rotation independently (so that are not affected by inter-calibration issues), as well as comparative results that can not be explained by the estimated systematic uncertainties:

- The structure of the electron density and the temperature of CR-2081 exhibit a remarkable N/S symmetry, both in the ES and CH regions. On the other hand, CR-1915 shows a N/S asymmetry, with its southern hemisphere exhibiting larger values of the electron density scale height and the electron temperature. Also, in each of the two analyzed rotations coronal holes

exhibit: a) sub-MK electron temperatures, and b) coronal base densities of order $\approx 1/2$ those in the low latitudes range of the equatorial streamer belt.

- Comparative ES study: In the low latitudes range CR-1915 exhibits an $\approx 8\%$ larger density than CR-2081, while difference in temperatures between both rotations are within the uncertainty level. In the southern hemisphere CR-1915 exhibits $\approx 20\%$ larger temperatures than CR-2081, as well as $\approx 25\%$ larger values of the scale density height. Also, in both rotations the characteristic values of the magnetic field strength are similar in the northern hemisphere, but in the southern hemisphere CR-1915 shows between 10 and 80% larger values than CR-2081, with increasing difference for larger latitudes.
- Comparative CH study: We limit this comparison to the southern CH due to data contamination in the northern off limb region of EIT 284 Å images. CR-1915 exhibits $\approx 20\%$ lower temperatures than CR-2081. In addition, the magnetic field strength of CR-1915 was considerably larger than for CR-2081, showing up to 50% larger values in the northern hemisphere and more than twice larger in the southern hemisphere.
- We have originally investigated the effect of the stray light removal in DEMT results in the case of EUVI. When its images are decontaminated there is a systematic increase of the resulting coronal base electron density by 7 to 15%, and a systematic decrease of the electron density scale height by 5 to 10%, depending on the coronal region. A similar analysis for EIT images is desirable but no quantitative characterization of its point-spread-function is available.

Characteristic density and temperature values found in the ES and CH regions of CR-2081, as well as their overall 3D distribution (radial gradients, latitudinal dependences, ES/CH contrast ratio, etc.) are fully consistent with previous DEMT studies related to the SC 23/24 minimum (Nuevo *et al.*, 2013; Vásquez, Frazin, and Manchester, 2010; Vásquez *et al.*, 2011). Being a period first analyzed here by means of the DEMT technique, we compare next the novel EIT-based results for the SC 22/23 minimum with other observational works concerning that period. Based on spectral data, the equatorial streamer structure has been studied below $1.2\,R_\odot$ during CRs 1912-1913 by Gibson *et al.* (1999) using the Coronal Diagnostic Spectrometer (CDS) onboard SOHO, and during CR-1916 by Feldman *et al.* (1999) using the Ultraviolet Measurement of Emitted Radiation (SUMER) instrument onboard SOHO. Compared to the results here reported for the similar region ES-Ll in Table 2, the electron densities reported by Gibson *et al.*are $\approx 50\%$ larger, and those reported by Feldman *et al.* are $\approx 25\%$ larger. Also, the temperatures reported by those studies at $r = 1.1\,R_\odot$ are in the range $\approx 1.3 - 1.4\,MK$, closely matching the characteristic $\approx 1.36\,MK$ temperature here reported for the ES-Ll region. These are remarkably consistent results, given the uncertainties involved in the aforementioned studies, which can build up to a factor of order ≈ 2 (Feldman *et al.*, 1999), specially taking into account the significant evolution that the atomic database and plasma emission models underwent since the dates of those previous works. Note also the $\approx 25\%$

difference between the results of the two cited studies, which may reflect true physical differences in the streamer belt plasma between CR-1912 and CR-1916.

Based on LASCO-C2/SOHO images, Lamy *et al.* (2014) carried out a comparative analysis of the coronal white light (WL) radiance during the last two solar minima, at considerably larger heights ($2.2-6.0\,R_\odot$) than our study, which focuses then on different coronal structures. Compared to the SC 22/23 minimum, they found the SC 23/24 minimum to have been fainter, with a radiance reduction of order $\approx$ 44% in the equatorial region, $\approx$ 17% in the northern hemisphere, and $\approx$ 29% in the southern hemisphere. As coronal WL radiance is proportional to its electron density, the results of their study are qualitatively consistent with ours, both in terms of the SC 22/23 minimum having been denser than the SC 23/24 one, as well in terms of the the N/S asymmetry observed in the SC 22/23 minimum.

The temperature structure of the magnetic field lines of the ES and CH regions was classified as type up/down (Section 4.1) or quasi-isothermal (QI, Section 4.2) upon their temperature radial gradient dT/dr being positive/negative or (nearly) zero (within the uncertainty of the data points). Next, we highlight conclusions from this analysis.

- QI loops are distributed roughly uniformly within the ES. An analysis of their density scale height and temperature suggests that the thermodynamical state of the low-latitudes of the ES region during CR-2081 was consistent with isothermal hydrostatic equilibrium solution, with higher latitudes showing less consistency. Overall CR-1915 results are less compatible with the hydrostatic state, consistently with this rotation belonging to a comparatively more active minimum epoch.
- Down loops are found in the low-latitudes of both rotations. In the case of CR-2081 our results compare very well with those of Nuevo *et al.* (2013). The results for CR-1915 are original, confirming that down loops seem to be expected in the core of the equatorial streamer belt in solar minimum conditions.
- In both rotations down loops are characterized by $\beta \gtrsim 1$ at the coronal base and above, while up loops are characterized by $\beta < 1$ (Table 5).

Down loops can be expected if coronal heating is strongly confined to the footpoints of the coronal structures (Serio *et al.*, 1981; Aschwanden and Schrijver, 2002). Until the original DEMT study by Huang *et al.* (2012) and the following one by Nuevo *et al.* (2013), down loops had not received much attention in a related observational and modeling literature mostly focused on the bright EUV and X-ray loops of AR regions. Nuevo *et al.* (2013) proposed a physical scenario to explain the presence of down loops, which involves the conversion of Alfvén waves into compressive modes, for which a plasma regime $\beta \gtrsim 1$ is required at the coronal base. Compressive modes are then efficiently damped at the transition region due to the local high sound speed gradient and thermal conduction, putting a large fraction of the heating at the coronal base. This proposed scenario has been recently theoretically explored by Schiff and Cranmer (2016), who performed simulations including mode conversion in a wide range of

coronal regimes. They have reproduced down loops and found that most ($> 99\%$) of the Alfvén waves need to be converted into compressive modes in order for the down loops to be stable. In our work we have confirmed the presence of down loops in both CR-2081 and CR-1915, and that they are characterized by the condition $\beta \gtrsim 1$ at the coronal base, required for efficient mode conversion and wave dissipation to take place at low heights.

In previous works DEMT has been used as a validation tool for 3D MHD simulations of the solar corona (Oran *et al.*, 2015; Jin *et al.*, 2012; van der Holst *et al.*, 2010) by means of the chromosphere/coronal model component of the Space Weather Modeling Framework (SWMF). Aiming at understanding the underlying physical reasons for the differences observed between the two analyzed rotations and, in particular, at reproducing the observed up/down structures, we will use the results of this work to validate SWMF simulations of the two analyzed rotations. To that end we will use the latest implementation of its chromosphere/coronal module, the Alfvén Wave Solar Model (AWSoM, van der Holst *et al.* 2014), which addresses the heating of the solar corona with low-frequency Alfvén wave turbulence. The simulations will be simultaneously validated at greater heights with 3D electron density maps derived from white light tomography based on LASCO/C2 images, which provide data in the height range $\approx 2.2 - 6.1\,\mathrm{R}_\odot$ (Frazin *et al.*, 2012). The two analyzed rotations constitute a sample from each of the last two solar minimum epochs. In a next stage we plan to carry out tomographic reconstruction and MHD simulation of other rotations selected from both periods. The aim is to characterize the thermodynamical 3D state of the inner corona during the two solar minima, as well as to perform systematic validation of the latest version of the AWSoM model.

Acknowledgments The authors wish to thank the two anonymous referees for their careful and critical review of the manuscript that helped to improve its content in a thorough fashion, particularly in relation to the explanation of physical aspects of the DEMT technique, and the significance of the systematic uncertainties involved in the analysis. The authors also wish to thank Dr. Enrico Landi and Dr. Frédéric Auchère for useful discussions. D.G.Ll. acknowledges CONICET doctoral fellowship (Res. Nro. 4870) to IAFE that supported his participation in this research. The authors acknowledge ANPCyT grant 2012/0973 and CONICET grant PIP # 11220120100403 to IAFE that partially supported their participation in this research.

Appendix

A. Uncertainty Analysis

Following the study developed by Nuevo *et al.* (2015), the systematic uncertainty of the results derived from the DEMT + PFSS study due to the tomography regularization level and the EUV images radiometric calibration is quantitatively investigated.

The EUVI and EIT data were prepared using the latest processing tools and calibration corrections provided by their teams through the SolarSoft package. The EUVI channels have an estimated relative radiometric calibration uncertainty between the different filters of order $\lesssim 15\%$ (Paper I), and the EIT

channels are thought to have a similar relative calibration uncertainty (Frédéric Auchère, private communication). Since the LDEM is sensitive to the ratios of the channel intensities, the relative calibration uncertainty propagates into the estimated electron density and temperature.

There is also an absolute radiometric calibration uncertainty for both telescopes, which corresponds to a common global factor that affects all channels simultaneously. Comparisons of EIT and EUVI observations indicate they agree to within about $\approx 30\%$ (Frédéric Auchère, private communication). For a practical comparison between the results based on data from both telescopes, we assume that each telescope's absolute radiometric calibration is half of that value, i.e. $\approx 15\%$. The effect of the absolute radiometric uncertainty is a global correction factor for the intensity of all EUV channels, and thus on the determined LDEM area. As the derived electron density scales with the square root of the LDEM, the absolute radiometric calibration uncertainty carries an uncertainty of order $\approx 8\%$ for the electron density, and has no effect on the determination of either the electron density scale height or the electron temperature (as they depend on the shape of the LDEM only, not its area).

The regularization level of the tomographic inversion is controlled by a single dimensionless amplitude parameter p called the regularization parameter. For $p = 0$ no regularization is applied. Its optimal value $p_{\rm opt}$ and its uncertainty Δp are determined through tomography cross validation studies (Frazin and Janzen, 2002; Frazin, Vásquez, and Kamalabadi, 2009) for each band independently. The resulting values depend on the particular instrument, band, and period under analysis. Based on the previous studies by Frazin, Vásquez, and Kamalabadi (2009); Vásquez, Frazin, and Manchester (2010); Vásquez *et al.* (2011) for EUVI data, by Nuevo *et al.* (2015) for SDO/AIA data, and our own studies for EIT data, for the present work characteristic average values are used for all EUV bands, specifically $p_{\rm opt} = 0.75$ and $\Delta p = 0.40$.

The effect of the sources of uncertainty into the results is then investigated through an "error box" analysis, consisting in varying the relevant parameters within their range of uncertainty in a controlled fashion. The DEMT analysis is applied to both over-regularized ($p = p_{\rm opt} + \Delta p$) and under-regularized ($p = p_{\rm opt} - \Delta p$) FBE sets, with the regularization level varied in unison for all bands. In each case, the relative radiometric uncertainty among the EUVI (or EIT) bands was simultaneously considered by applying a $\pm 15\%$ relative correction to the FBE values of each band. As three EUV bands are used, the possible combinations for this relative correction are $C = 2^3$. In summary, for each rotation, C under-regularized and C over-regularized DEMT studies are performed, with each of the $N = 2C$ cases corresponding to a "corner" case of the error box analysis.

For each of the resulting N DEMT data sets the analysis is performed. For each coronal region, the median value of the N statistical distributions of each analyzed physical parameter ($N_{\rm CM}$, λ_N, $\langle T_m \rangle$) can be computed. Then, the mean value and standard deviation (over all N studies) of those medians is obtained. The results are fully detailed in the first three columns of Tables 7 and 8, for rotations CR-2081 and CR-1915, respectively. For each coronal region, the first row summarizes the "base" DEMT results reported in the paper (i.e.,

without applying corrections to the FBEs). The second row shows the average μ of the results of the N DEMT + PFFS studies, while the third row shows their fractional standard deviation σ/μ. This fractional standard deviation is a measure of the uncertainty of the corresponding physical parameter due to the systematic uncertainties. The last three columns show the results for the fractional standard deviation of the N statistical distributions of each analyzed physical parameter. The results of the tables are discussed in Section 3.6.

Table 7. Results of the error box analysis (see text) of for CR-2081, based on EUVI data. For each coronal region, the first row shows the "base" value (see text) of the median and fractional standard deviation the derived physical parameters ($N_{\rm CB}$, λ_N and $\langle T_m \rangle$). For each region, the second and third rows show the corresponding mean μ and fractional standard deviation σ/μ values, taken over the N DEMT + PFSS studies, as described in the text.

Region		Md($N_{\rm CB}$)	Md(λ_N)	Md($\langle T_m \rangle$)	$\frac{\rm SD(N_{CB})}{\rm Mn(N_{CB})}$	$\frac{\rm SD(\lambda_N)}{\rm Mn(\lambda_N)}$	$\frac{\rm SD\langle T_m \rangle}{\rm Mn(\langle T_m \rangle)}$
	base	0.936	0.070	0.911	0.109	0.128	0.032
CH-NH	μ	0.934	0.071	0.913	0.117	0.136	0.034
	σ/μ	0.031	0.016	0.041	0.156	0.087	0.151
	base	1.047	0.080	1.060	0.315	0.290	0.181
CH-Nl	μ	1.081	0.081	1.092	0.314	0.305	0.176
	σ/μ	0.022	0.015	0.078	0.053	0.099	0.161
	base	1.327	0.094	1.331	0.188	0.238	0.068
ES-Nb	μ	1.349	0.094	1.331	0.188	0.239	0.069
	σ/μ	0.044	0.010	0.035	0.059	0.151	0.204
	base	1.577	0.085	1.374	0.172	0.292	0.095
ES-Nm	μ	1.593	0.084	1.374	0.172	0.304	0.095
	σ/μ	0.025	0.025	0.030	0.049	0.128	0.161
	base	1.731	0.079	1.179	0.159	0.262	0.122
ES-Ll	μ	1.733	0.079	1.182	0.168	0.274	0.120
	σ/μ	0.022	0.012	0.059	0.110	0.083	0.123
	base	1.594	0.081	1.356	0.176	0.268	0.090
ES-Sm	μ	1.605	0.080	1.353	0.178	0.279	0.090
	σ/μ	0.025	0.014	0.033	0.063	0.046	0.182
	base	1.238	0.093	1.385	0.183	0.241	0.088
ES-Sb	μ	1.244	0.094	1.385	0.186	0.249	0.086
	σ/μ	0.019	0.014	0.027	0.061	0.125	0.172
	base	0.900	0.086	1.046	0.245	0.271	0.169
CH-Sl	μ	0.924	0.087	1.063	0.239	0.272	0.168
	σ/μ	0.046	0.029	0.072	0.030	0.092	0.141
	base	0.882	0.071	0.930	0.147	0.159	0.052
CH-Sh	μ	0.886	0.070	0.930	0.152	0.178	0.052
	σ/μ	0.031	0.022	0.035	0.227	0.213	0.130

Table 8. Same as Table 7 but for CR-1915, based on EIT data.

Region		Md($N_{\rm CB}$)	Md(λ_N)	Md($\langle T_m \rangle$)	$\frac{\rm SD(N_{CB})}{\rm Mn(N_{CB})}$	$\frac{\rm SD(\lambda_N)}{\rm Mn(\lambda_N)}$	$\frac{\rm SD\langle T_m \rangle}{\rm Mn(\langle T_m \rangle)}$
CH-Nh	base	0.829	0.094	0.723	0.192	0.219	0.261
	μ	0.829	0.096	0.725	0.195	0.230	0.278
	σ/μ	0.035	0.025	0.026	0.100	0.109	0.134
CH-Nl	base	1.000	0.101	1.019	0.308	0.300	0.444
	μ	1.031	0.100	1.065	0.301	0.298	0.436
	σ/μ	0.041	0.022	0.200	0.036	0.102	0.242
ES-Nb	base	1.484	0.093	1.441	0.122	0.199	0.193
	μ	1.490	0.092	1.413	0.121	0.222	0.218
	σ/μ	0.032	0.018	0.078	0.164	0.241	0.274
ES-Nm	base	1.651	0.082	1.459	0.163	0.257	0.143
	μ	1.669	0.082	1.436	0.168	0.282	0.151
	σ/μ	0.035	0.037	0.078	0.043	0.194	0.315
ES-Ll	base	1.863	0.081	1.356	0.127	0.208	0.176
	μ	1.870	0.081	1.322	0.130	0.217	0.193
	σ/μ	0.023	0.012	0.115	0.141	0.110	0.354
ES-Sm	base	1.595	0.100	1.630	0.183	0.312	0.140
	μ	1.617	0.099	1.615	0.185	0.311	0.144
	σ/μ	0.033	0.013	0.037	0.061	0.052	0.285
ES-Sb	base	1.155	0.118	1.619	0.251	0.345	0.198
	μ	1.204	0.117	1.613	0.243	0.312	0.213
	σ/μ	0.076	0.034	0.045	0.057	0.052	0.228
CH-Sl	base	0.934	0.085	0.803	0.254	0.554	0.258
	μ	0.948	0.086	0.804	0.248	0.439	0.230
	σ/μ	0.085	0.058	0.045	0.082	0.198	0.356
CH-Sh	base	0.852	0.094	0.772	0.172	0.216	0.085
	μ	0.859	0.094	0.779	0.180	0.227	0.091
	σ/μ	0.034	0.035	0.032	0.125	0.061	0.256

Disclosure of Potential Conflicts of Interest: The authors declare that they have no conflicts of interest.

References

Altschuler, M.D., Perry, R.M.: 1972, On Determining the Electron Density Distribution of the Solar Corona from K-Coronameter Data. *Solar Phys.* **23**, 410. DOI. ADS.

Aschwanden, M.J., Boerner, P.: 2011, Solar Corona Loop Studies with the Atmospheric Imaging Assembly. I. Cross-sectional Temperature Structure. *Astrophys. J.* **732**, 81. DOI. ADS.

Aschwanden, M.J., Schrijver, C.J.: 2002, Analytical Approximations to Hydrostatic Solutions and Scaling Laws of Coronal Loops. *Astrophys. J.* **142**, 269. DOI. ADS.

Biesecker, D.A., Thompson, B.J., Gibson, S.E., Alexander, D., Fludra, A., Gopalswamy, N., Hoeksema, J.T., Lecinski, A., Strachan, L.: 1999, Synoptic Sun during the first Whole Sun Month Campaign: August 10 to September 8, 1996. *J. Geophys. Res.* **104**, 9679. DOI. ADS.

Butala, M.D., Hewett, R.J., Frazin, R.A., Kamalabadi, F.: 2010, Dynamic Three-Dimensional Tomography of the Solar Corona. *Solar Phys.* **262**, 495. DOI. ADS.

Cheung, M.C.M., Boerner, P., Schrijver, C.J., Testa, P., Chen, F., Peter, H., Malanushenko, A.: 2015, Thermal Diagnostics with the Atmospheric Imaging Assembly on board the Solar Dynamics Observatory: A Validated Method for Differential Emission Measure Inversions. *Astrophys. J.* **807**, 143. DOI. ADS.

Del Zanna, G.: 2013, The multi-thermal emission in solar active regions. *Astron. Astrophys.* **558**, A73. DOI. ADS.

Feldman, U., Mandelbaum, P., Seely, J.F., Doschek, G.A., Gursky, H.: 1992, The potential for plasma diagnostics from stellar extreme-ultraviolet observations. *Astrophys. J. Suppl.* **81**, 387. DOI. ADS.

Feldman, U., Doschek, G.A., Schühle, U., Wilhelm, K.: 1999, Properties of Quiet-Sun Coronal Plasmas at Distances of $1.03 \leq R_{\odot} \leq 1.50$ along the Solar Equatorial Plane. *Astrophys. J.* **518**, 500. DOI. ADS.

Frazin, R.A.: 2000, Tomography of the Solar Corona. I. A Robust, Regularized, Positive Estimation Method. *Astrophys. J.* **530**, 1026. DOI. ADS.

Frazin, R.A., Janzen, P.: 2002, Tomography of the Solar Corona. II. Robust, Regularized, Positive Estimation of the Three-dimensional Electron Density Distribution from LASCO-C2 Polarized White-Light Images. *Astrophys. J.* **570**, 408. DOI. ADS.

Frazin, R.A., Vásquez, A.M., Kamalabadi, F.: 2009, Quantitative, Three-dimensional Analysis of the Global Corona with Multi-spacecraft Differential Emission Measure Tomography. *Astrophys. J.* **701**, 547. DOI. ADS.

Frazin, R.A., Vásquez, A.M., Thompson, W.T., Hewett, R.J., Lamy, P., Llebaria, A., Vourlidas, A., Burkepile, J.: 2012, Intercomparison of the LASCO-C2, SECCHI-COR1, SECCHI-COR2, and Mk4 Coronagraphs. *Solar Phys.* **280**, 273. DOI. ADS.

Gibson, S.E., Fludra, A., Bagenal, F., Biesecker, D., del Zanna, G., Bromage, B.: 1999, Solar minimum streamer densities and temperatures using Whole Sun Month coordinated data sets. *J. Geophys. Res.* **104**, 9691. DOI. ADS.

Hannah, I.G., Kontar, E.P.: 2012, Differential emission measures from the regularized inversion of Hinode and SDO data. *Astron. Astrophys.* **539**, A146. DOI. ADS.

Huang, Z., Frazin, R.A., Landi, E., Manchester, W.B., Vásquez, A.M., Gombosi, T.I.: 2012, Newly Discovered Global Temperature Structures in the Quiet Sun at Solar Minimum. *Astrophys. J.* **755**, 86. DOI. ADS.

Jin, M., Manchester, W.B., van der Holst, B., Gruesbeck, J.R., Frazin, R.A., Landi, E., Vasquez, A.M., Lamy, P.L., Llebaria, A., Fedorov, A., Toth, G., Gombosi, T.I.: 2012, A Global Two-temperature Corona and Inner Heliosphere Model: A Comprehensive Validation Study. *Astrophys. J.* **745**, 6. DOI. ADS.

Kashyap, V., Drake, J.J.: 1998, Markov-Chain Monte Carlo Reconstruction of Emission Measure Distributions: Application to Solar Extreme-Ultraviolet Spectra. *Astrophys. J.* **503**, 450. DOI. ADS.

Lamy, P., Barlyaeva, T., Llebaria, A., Floyd, O.: 2014, Comparing the solar minima of cycles 22/23 and 23/24: The view from LASCO white light coronal images. *Journal of Geophysical Research (Space Physics)* **119**, 47. DOI. ADS.

Landi, E., Feldman, U., Dere, K.P.: 2002, CHIANTI - An Atomic Database for Emission Lines. V. Comparison with an Isothermal Spectrum Observed with SUMER. *Astrophys. J. Suppl.* **139**, 281. DOI. ADS.

Landi, E., Young, P.R., Dere, K.P., Del Zanna, G., Mason, H.E.: 2013, CHIANTI - An Atomic Database for Emission Lines. XIII. Soft X-Ray Improvements and Other Changes. *Astrophys. J.* **763**, 86. DOI. ADS.

Li, J., Raymond, J.C., Acton, L.W., Kohl, J.L., Romoli, M., Noci, G., Naletto, G.: 1998, Physical Structure of a Coronal Streamer in the Closed-Field Region as Observed from UVCS/SOHO and SXT/Yohkoh. *Astrophys. J.* **506**, 431. DOI. ADS.

Lloveras, D.G., Vásquez, A.M., Shearer, P., Frazin, R.A.: 2017, Effect of Stray Light Correction of Extreme-ultraviolet Solar Images in Tomography. *Boletín de la Asociacion Argentina de Astronomia La Plata Argentina, submitted.*

Nerney, S., Suess, S.T.: 2005, Stagnation Flow in Thin Streamer Boundaries. *Astrophys. J.* **624**, 378. DOI. ADS.

Nuevo, F.A., Huang, Z., Frazin, R., Manchester, W.B. iv, Jin, M., Vásquez, A.M.: 2013, Evolution of the Global Temperature Structure of the Solar Corona during the Minimum between Solar Cycles 23 and 24. *Astrophys. J.* **773**, 9. DOI. ADS.

Nuevo, F.A., Vásquez, A.M., Landi, E., Frazin, R.: 2015, Multimodal Differential Emission Measure in the Solar Corona. *Astrophys. J.* **811**, 128. DOI. ADS.

Oran, R., Landi, E., van der Holst, B., Lepri, S.T., Vásquez, A.M., Nuevo, F.A., Frazin, R., Manchester, W., Sokolov, I., Gombosi, T.I.: 2015, A Steady-state Picture of Solar Wind Acceleration and Charge State Composition Derived from a Global Wave-driven MHD Model. *Astrophys. J.* **806**, 55. DOI. ADS.

Plowman, J., Kankelborg, C., Martens, P.: 2013, Fast Differential Emission Measure Inversion of Solar Coronal Data. *Astrophys. J.* **771**, 2. DOI. ADS.

Schiff, A.J., Cranmer, S.R.: 2016, Explaining Inverted-temperature Loops in the Quiet Solar Corona with Magnetohydrodynamic Wave-mode Conversion. *Astrophys. J.* **831**, 10. DOI. ADS.

Schmelz, J.T., Christian, G.M., Chastain, R.A.: 2016, The Coronal Loop Inventory Project: Expanded Analysis and Results. *Astrophys. J.* **831**, 199. DOI. ADS.

Serio, S., Peres, G., Vaiana, G.S., Golub, L., Rosner, R.: 1981, Closed coronal structures. II - Generalized hydrostatic model. *Astrophys. J.* **243**, 288. DOI. ADS.

Shearer, P., Frazin, R.A., Hero, A.O. III, Gilbert, A.C.: 2012, The First Stray Light Corrected Extreme-ultraviolet Images of Solar Coronal Holes. *Astrophys. J. Lett.* **749**, L8. DOI. ADS.

Suess, S.T., Wang, A.-H., Wu, S.T.: 1996, Volumetric heating in coronal streamers. *J. Geophys. Res.* **101**, 19957. DOI. ADS.

Tóth, G., van der Holst, B., Huang, Z.: 2011, Obtaining Potential Field Solutions with Spherical Harmonics and Finite Differences. *Astrophys. J.* **732**, 102. DOI. ADS.

van der Holst, B., Manchester, W.B. IV, Frazin, R.A., Vásquez, A.M., Tóth, G., Gombosi, T.I.: 2010, A Data-driven, Two-temperature Solar Wind Model with Alfvén Waves. *Astrophys. J.* **725**, 1373. DOI. ADS.

van der Holst, B., Sokolov, I.V., Meng, X., Jin, M., Manchester, W.B. IV, Tóth, G., Gombosi, T.I.: 2014, Alfvén Wave Solar Model (AWSoM): Coronal Heating. *Astrophys. J.* **782**, 81. DOI. ADS.

Vásquez, A.M.: 2016, Seeing the solar corona in three dimensions. *Advances in Space Research* **57**, 1286. DOI.

Vásquez, A.M., Frazin, R.A., Kamalabadi, F.: 2009, 3D Temperatures and Densities of the Solar Corona via Multi-Spacecraft EUV Tomography: Analysis of Prominence Cavities. *Solar Phys.* **256**, 73. DOI. ADS.

Vásquez, A.M., Frazin, R.A., Manchester, W.B. IV: 2010, The Solar Minimum Corona from Differential Emission Measure Tomography. *Astrophys. J.* **715**, 1352. DOI. ADS.

Vásquez, A.M., van Ballegooijen, A.A., Raymond, J.C.: 2003, The Effect of Proton Temperature Anisotropy on the Solar Minimum Corona and Wind. *Astrophys. J.* **598**, 1361. DOI. ADS.

Vásquez, A.M., Huang, Z., Manchester, W.B., Frazin, R.A.: 2011, The WHI Corona from Differential Emission Measure Tomography. *Solar Phys.* **274**, 259. DOI. ADS.

Vibert, D., Peillon, C., Lamy, P., Frazin, R.A., Wojak, J.: 2016, Time-dependent tomographic reconstruction of the solar corona. *Astronomy and Computing* **17**, 144. DOI. ADS.

Wang, Y.-M., Sheeley, N.R. Jr., Walters, J.H., Brueckner, G.E., Howard, R.A., Michels, D.J., Lamy, P.L., Schwenn, R., Simnett, G.M.: 1998, Origin of Streamer Material in the Outer Corona. *Astrophys. J. Lett.* **498**, L165. DOI. ADS.

Warren, H.P., Byers, J.M., Crump, N.A.: 2017, Sparse Bayesian Inference and the Temperature Structure of the Solar Corona. *Astrophys. J.* **836**, 215. DOI. ADS.